Check for updates

CrystEngComm

Accepted Manuscript

CrystEngComm

rsc.li/crystengcomm

ROYAL SOCIETY
OF CHEMISTRY

PAPER
Yuan Zhuang et al
Structural study on PVA assisted self-assembled 3D
hierarchical iron (hydr)oxides

This is an Accepted Manuscript, which has been through the Royal Society of Chemistry peer review process and has been accepted for publication.

Accepted Manuscripts are published online shortly after acceptance, before technical editing, formatting and proof reading. Using this free service, authors can make their results available to the community, in citable form, before we publish the edited article. We will replace this Accepted Manuscript with the edited and formatted Advance Article as soon as it is available.

You can find more information about Accepted Manuscripts in the Information for Authors.

Please note that technical editing may introduce minor changes to the text and/or graphics, which may alter content. The journal's standard Terms & Conditions and the Ethical guidelines still apply. In no event shall the Royal Society of Chemistry be held responsible for any errors or omissions in this Accepted Manuscript or any consequences arising from the use of any information it contains.

ROYAL SOCIETY
OF CHEMISTRY

rsc.li/crystengcomm

ARTICLE

From solid solution towards pyrochlore and kappa phases: introducing configurational entropy in ordered ceria-zirconia systems

Stjepan Šarić[a], Dalibor Tatar[a], Tina Skalar[b], Marjan Marinšek[b], Cora Bartus Pravda[c], Ákos Kukovecz[c], Imre Szenti[c], Matjaž Finšgar[d], Igor Djerdj[a] and Jelena Kojčinović[a,*]

Following the example of well-known ceria-zirconia pyrochlore and kappa structures, the high-entropy rare-earth counterparts were synthesized. To synthesize ceria-zirconia-based solid solutions, the modified aqueous citrate sol-gel method was applied. In order to obtain pyrochlore phases, reduction by hydrogen (3% H_2 in Ar) was needed at a high temperature of around 1500 °C. The last step included mild re-oxidation at around 600 °C under atmospheric conditions to accomplish kappa phases of a high degree of ordering. A direct comparison of different phases of CeZrO and its high-entropy counterpart LCPGY compounds was studied. Their structural similarities and differences were investigated using powder X-ray diffraction (PXRD), Raman spectroscopy, scanning electron microscopy with energy dispersive X-ray spectroscopy (SEM-EDS), and physisorption measurements. Using thermogravimetric analysis (TGA), the thermal behaviour was inspected, which showed direct transformation of pyrochlore to kappa phase due to oxygen uptake, i.e. mass gain. The surfaces of the compounds were analysed by X-ray photoelectron spectroscopy (XPS) to investigate Ce^{3+}/Ce^{4+}, O_{ads}/O_{total}, and Pr^{3+}/Pr_{total} ratios. Temperature programmed desorption (TPD) using 5% CH_4/Ar was conducted to show the catalytic activity of the synthesized compounds towards methane oxidation. Introducing configurational entropy in ordered ceria-zirconia systems showed that to obtain single-phase pyrochlore and kappa phases, it is also necessary to pay attention to the reduction/oxidation time and temperature, in addition to the radius ratio, oxidation states, and atomic size disorder. Guided by this theory and experimental findings, we propose that the synthesized pyrochlore high-entropy compound is dual-phase pyrochlore and fluorite, while its kappa form is actually partially oxidized single-phase pyrochlore. High-entropy forms of synthesized compounds showed much better catalytic performance towards methane oxidation than their non-high-entropy counterparts.

Introduction

Ceria-zirconia (CeO_2-ZrO_2) system has attracted attention in the last decade due to its mechanical, electrical, and thermal properties[1], but also a wide variety of applications of zirconia-ceria-based materials in areas such as electronics[2], engineering[3], catalysis[4], nanomedicine[5], fuel cells[6], etc. By adding a small amount (10-12 mol%) of cerium (IV) oxide, the tetragonal zirconia phase stabilizes over the fact that quite extensive Ce^{4+} ions expand the cation network[7]. On the other hand, zirconium atoms are credited for the thermal stabilization of CeO_2 in terms of increased resistance to sintering[8,9] and structural stabilization[9]. Due to their enormous chemical and thermal stability, CeO_2-ZrO_2-based materials are widely used as

catalysts in the treatment of emission gases, which is justified by the fact that the oxygen storage/release capacity (OSC) of CeO_2 is enhanced by adding Zr into the structure[10] Another huge advantage is that Ce atoms can effortlessly change the oxidation state between Ce^{3+} and Ce^{4+} cations[11].

In previous years, mixed Ce-Zr (1:1) oxide, the so-called solid solution t-$Ce_{0.5}Zr_{0.5}O_2$, was shown to be more catalytically active and overall stable than pure CeO_2 or tetragonal ZrO_2[12]. Since the catalytic activity of these materials depends on oxygen storage capacity, transforming a solid solution t-$Ce_{0.5}Zr_{0.5}O_2$ to "kappa phase ", κ-$Ce_2Zr_2O_8$, enhances oxidation-reduction processes significantly[13]. This high oxygen storage capacity is due to an ordered array of cations in a cubic lattice of κ-$Ce_2Zr_2O_8$, which is why 1/8 of the oxygen anions can freely be removed. In order to prepare "kappa phase "κ-$Ce_2Zr_2O_8$, the solid solution t-$Ce_{0.5}Zr_{0.5}O_2$ has to be reduced by hydrogen at high temperature, which is around 1500 °C[14,15], to obtain the pyrochlore phase p-$Ce_2Zr_2O_7$. Pyrochlore $Ce_2Zr_2O_7$ could also be described as an anion-deficient distorted fluorite structure with two cations of different radii and 1/8 of empty tetrahedral anionic positions[14,15]. These empty positions are so-called oxygen vacancies, which smooth the way for the cations' ordering and consequently the ordering of the cationic sublattice.

a. Department of Chemistry, Josip Juraj Strossmayer University of Osijek, Cara Hadrijana 8/A, 31000 Osijek, Croatia, jbijelic@kemija.unios.hr
b. Faculty of Chemistry and Chemical Technology, Večna pot 113, 1000 Ljubljana, Slovenia
c. Department of Applied and Environmental Chemistry, University of Szeged, 6720 Szeged, Hungary
d. Faculty of Chemistry and Chemical Engineering, University of Maribor, Maribor Smetanova 17, 2000, Slovenia
† Supplementary Information available:. See DOI: 10.1039/x0xx00000x

ARTICLE

CrystEngComm

High-entropy materials have been thoroughly investigated since their discovery in 2015 by Rost et al.[16] and they have been the centre of scientific research in materials chemistry. The reason behind this is the diversity of possible elemental combinations that can be used to produce such materials. Another reason is that high entropy induces defects on the surface of such materials that open up new pathways to possible fundamental and applicative research[17]. Introducing high-entropy into ordered ceria-zirconia systems using rare earth elements gives a whole new class of materials known as high-entropy ceramics. In particular, high-entropy rare earth zirconates ($RE_2Zr_2O_7$) are widely known due to their extraordinary thermophysical properties, catalytic performances, irradiation resistance, etc[18–20]. Li et al.[21] reported a study of single- and dual-phase rare-earth zirconate high-entropy ceramics, which showed that these types of materials could be used for thermal barrier coatings. The results showed that incorporating multiple rare-earth elements onto the A site of pyrochlore structures, higher thermal expansions and mechanical properties are obtained compared to single rare earth zirconates, $RE_2Zr_2O_7$. In order to obtain these kinds of compounds, three main conditions have to be satisfied. Firstly, the pyrochlore crystal structure is controlled by the cation radius ratio r_A/r_B which has to be between 1.46-1.78[22,23], where the A site in this case belongs to trivalent rare earth cations and the B site is occupied by tetravalent zirconium cation. On the other hand, defective fluorite structure and monoclinic structure are obtained if r_A/r_B ratio is lower or higher than this scale[22,23]. Secondly, to define these materials as high-entropy, single-phase system has to contain 5 or more cations, the configurational entropy (S_{conf}) has to be greater than or equal to $1.5R$[24,25], where R is the ideal gas constant. The third, but also the most important factor influencing the formation of single-phase pyrochlore structure is atomic size difference (disorder), known as δ, which was first employed by Zhang et al[26]. It represents the ionic radius difference of the A site in high-entropy pyrochlore/fluorite oxides and gives an answer whether a single or dual-phase is formed in high-entropy rare earth zirconates. The general formula is described by **Equation (1)**:

$$\delta = \sqrt{\sum c_i (1 - \frac{r_i}{r})^2} \qquad (1)$$

where c_i and r_i represent the atomic percent and ionic radius of element i at the corresponding site, and r is the average ionic radius. In case of pyrochlore, two cation sublattices exist, so it is mandatory to calculate the size disorder (δ) of the cations of both sites, A and B. When talking about zirconates, there is only a zirconium cation on the B site; thus, the prediction of structure type depends only on the size disorder of the A site. Wang et al.[27] synthesized eighteen different 5-component equimolar rare earth zirconates following these three main criteria. The size disorder for all the compounds was the main factor in obtaining single-phase zirconate since the study showed that the size disorder value greater than 5 forms a dual-phase compound in pyrochlore/fluorite systems, regardless of the radius ratio.

In order to predict stability and customize synthesis path of rare-earth high-entropy oxides, it is indispensable to understand the interaction of parameters such as valence state, ionic size of the constituent cations, preferred coordination and thermal properties[28]. Rare-earth oxides commonly crystallize in fluorite or bixbyite forms, with CeO_2 serving as a standard fluorite-phase oxide. The main differences between these two structures are that bixbyite structure is a derivative of the fluorite structure, having doubled lattice parameter and more unoccupied anion sites. Fluorite structure favors rare-earth cations with higher oxidation state (+4) and eightfold coordination, while bixbyite relies on lower oxidation state (+3) and sixfold coordination[29]. Sarkar et al.[30] synthesized equiatomic rare earth oxides with up to seven different cations and showed that using rare-earth cations with higher oxidation state (+4), contributes to fluorite structure. Also, by increasing the concentration of cerium cation, fluorite structure is favored. All these parameters need to be satisfied in order to find the optimal synthesis conditions to produce rare-earth high-entropy oxides with fluorite structure, such as in CeO_2[31].

Since bixbyite and pyrochlore structures both favour +3 oxidation state, it is possible to oxidize them leading to formation of other different phases. Bixbyite structure is quite stable and its oxidation can lead to an increase of lattice disorder and oxygen vaccancy concentration[31,32]. However, in high-entropy oxides, a phase transition could occur from bixbyite to fluorite structure as a result of increase of configurational entropy[29,33].

On the contrary, reduction of equimolar ceria-zirconia solid solution leads to formation of ordered pyrochlore structure which is irreversible since re-oxidation of pyrochlore leads to symmetry breaking and formation of oxygen-rich kappa phase[14,15]. To the best of our knowledge, there are no references in the literature regarding the high-entropy kappa form ($A_2B_2O_8$) of rare-earth zirconates.

Since nanocrystalline ceria-zirconia-based compounds exhibit oxygen-rich surfaces that can be used in oxidation reactions, they are often used in the methane oxidation process[34–41]. Methane is a greenhouse gas that affects the climate, so it is undesirable in the atmosphere, even though it is a primary component of natural gas. It can be partially oxidized to methanol, carbon monoxide, or fully oxidized to carbon dioxide, which depends on the targeted use. Although carbon dioxide is also a greenhouse gas, it has found application in industry. It is mostly used in agriculture in urea production. Still, it is also used to enhance fossil fuel recovery, as a food additive (especially in carbonated drinks, but also as an acidity regulator and propellant), fire extinguishers, refrigerants, as a solvent in its supercritical state, etc. This is why it is important to have controlled carbon dioxide production as a raw material for further applications.

In this work, we synthesized solid solution $Ce_{0.5}Zr_{0.5}O_2$ and its high-entropy counterpart $La_{0.1}Ce_{0.1}Pr_{0.1}Gd_{0.1}Y_{0.1}Zr_{0.5}O_2$ using the citrate-nitrate route previously developed by our group[42–48]. Then, controlled reduction of the starting solid solution was

performed to produce the pyrochlore form, $A_2Zr_2O_7$. Further, re-oxidation of the reduced pyrochlore form was conducted to produce the kappa phase, $A_2Zr_2O_8$. Obtained compounds were subjected to structural and microstructural analysis, and insight into the application of these compounds in methane oxidation was given.

Experimental

Materials and methods

Synthesis. The following chemicals were used without further purification: Citric acid monohydrate (T.T.T., Croatia), concentrated ammonia solution (Gram-Mol, Croatia), cerium(III) nitrate hexahydrate (Acros Organics, USA), lanthanum(III) nitrate hexahydrate (Sigma Aldrich, USA), yttrium nitrate(III) hexahydrate (Alfa Aesar, USA), praseodymium(III) nitrate hexahydrate (Sigma Aldrich, USA) and gadolinium(III) nitrate hexahydrate (Acros Organics, USA). Zirconium oxynitrate hydrate (Sigma Aldrich, USA) was dried at 80 °C overnight before use in the drying oven Instrumentaria ST-01/02.

Powder X-ray diffraction. Powder X-ray diffraction was carried out using a Panalytical Aeris Research diffractometer with a CuKα (λ = 1.54059 Å) radiation source in an ambient atmosphere. Method for the collection of XRD data included a step size of 0.002°, 20.4 s per step, a divergence slit of 1°, and a fixed mask of 13 mm. The diffractograms were recorded in the range 2θ from 10° up to 90°.

Raman spectroscopy. Raman spectroscopy was performed using a Bruker Confocal microscope Sentera II with a 532 nm wavelength source and a laser power of 2.50 mW. The spectral resolution was 4 cm^{-1}, optical objective 50x, aperture 50x1000 μm, and 3 co-additions of 10000 ms for each measurement.

Scanning electron microscopy. The morphological characterization and elemental composition of powder samples were observed by the Thermo Fischer Scientific Apreo 2S field emission scanning electron microscope (FE-SEM). The optimal resolution was ensured by operating at an acceleration voltage of 2 kV and a working distance set to approximately 5.5 mm. Images were obtained by secondary electron (SE) and backscattered (BSE) detectors.

Energy dispersive X-ray spectroscopy. Qualitative and quantitative analysis of observed powders was performed at 20 kV using an energy dispersive detector (EDS) an Oxford X-Max SDD 100 mm^{2,} and AZtec X-ray microanalysis software, thereby facilitating comprehensive elemental mappings and compositions.

X-ray photoelectron spectroscopy. XPS analysis was carried out using a Supra+ (Kratos, Manchester, UK) coupled with an Al K$_\alpha$ X-ray excitation source. The charge neutralizer was active during the measurements. The take-off angle was set at 90°. Powder samples were placed on a carbon tape mounted on a silicon wafer. Measurements were executed at a pass energy of 20 eV. Data acquisition and analysis were performed using ESCApe 1.5 software (Kratos). The binding energy scale was corrected to the C-C/C-H peak at 284.8 eV in the C 1s spectrum.

Thermogravimetric analysis. TGA measurements were performed using a Netzsch STA 449 F3 Jupiter system. The experimental protocol started with an isothermal phase at 30 °C for 1 h. Subsequently, the samples were subjected to a controlled heating phase to 600 °C using a 2.5 °C min^{-1} heating rate and finalised in an isothermal step at peak temperature for 4 h. All segments were performed using Ar 5.0 atmosphere with a 100 mL min^{-1} flow rate and an Al_2O_3 crucible as reference material. Additionally, pyrochlore phases were also conducted in an oxygen atmosphere under the same temperature conditions.

Temperature-programmed desorption. Thermal deposition with methane of powder samples was analysed in four steps, using 5 vol.% CH_4/Ar 5.0 atmosphere with a 100 mL min^{-1} flow rate. Starting with heating from an initial 50 to 400 °C using a heating rate of 10 °C min^{-1}, followed by the first thermostating at 400 °C for 30 min. The third phase was additionally heating to 700 °C with a heating rate of 10 °C min^{-1} and finalized with the second isothermal step at 700 °C for 3h. All measurements were simultaneously analysed for evolved gas analysis (EGA) using a quadrupole mass spectrometer (QMS) model 403C Aëolos.

Specific surface area. Nitrogen adsorption-desorption isotherms for all powder samples were recorded at a temperature of −196 °C using Autosorb IQ (Quantachrome Instruments USA), a surface gas sorption analyser. Before starting the adsorption measurements, the samples were degassed at a temperature of 250 °C under vacuum for 12 hours in order to remove all moisture and impurities from the pores.

Powder preparation

Synthesis of solid solution powders. The modified aqueous citrate sol-gel method was used for the synthesis of ceria-zirconia-based solid solutions $Ce_{0.5}Zr_{0.5}O_2$ and $La_{0.1}Ce_{0.1}Pr_{0.1}Gd_{0.1}Y_{0.1}Zr_{0.5}O_2$. Stoichiometric amounts of nitrate precursors (**Table S1**) of the involved cations were dissolved in a citric acid solution (w = 10 %) using MiliQ water (prepared by the PURELAB Flex device). A pH value adjustment to 5 was carried out with a HANNA pH 211 device using a concentrated ammonia solution (w = 25 %). Prepared reaction solutions were heated up to 95°C (solution temperature) on a magnetic hotplate stirrer DLAB MS-H-S under continuous stirring until a black resin was formed. The obtained black resin was dried in a drying oven (Instrumentaria ST-01/02) at 120°C overnight to produce a xerogel-like mixture. Calcination of the xerogel-like mixture was performed up to 600°C (heating rate 2°C/min) for 8 h using Nabertherm LT5/11/B410 muffle furnace.

Reduction of solid solution powders. Solid solution powders were subjected to a reduction in a Carbolite Gero TF1 16/60/180 high-temperature tube furnace with a Eurotherm EPC 3016 controller to obtain pyrochlore phases. Small amounts of powder were placed in a rectangular crucible in the tube. Powders were then heated in an inert N_2 atmosphere (gas flow 300 mL/min) up to 800 °C (heating rate 4.5 °C/min) to eliminate the air from the tube. Then, the atmosphere was changed to 3% H_2 in Ar (gas flow 300 mL/min) from 800 °C to 1000 °C (4.5

°C/min). The heating was then continued from 1000 °C to 1500 °C under the same reducing atmosphere but with a heating rate of 1 °C/min. Then, the powders were left at 1500 °C in the reducing atmosphere (3% H_2 in Ar) for 10 hours. After that, the cooling process took place: first from 1500 °C to 800 °C under a 3 % H_2 in Ar atmosphere (10 °C/min) and finally from 800 °C to room temperature under a N_2 atmosphere.

Re-oxidation of the reduced powders. Re-oxidation of the reduced powders was performed to obtain κ-phases. Reduced powders were placed in a crucible in a muffle furnace (Nabertherm LT5/11/B410), heated up to 600 °C with a heating rate of 2.5 °C/min for 4 hours (stabilization time). Cooling took place inside the furnace.

All of the above-mentioned steps are visualized in **Scheme 1**. Synthesized compounds were classified into three groups: 1) starting oxides (solid solutions), 2) reduced forms (pyrochlore phases), and 3) re-oxidized forms (kappa phases). Their code names are summarized in **Table 1**.

Table 1. List of prepared compounds and their code names.

Powder	Composition	Code name	Note
Starting oxide (solid solution)	$Ce_{0.5}Zr_{0.5}O_2$	CeZrO	–
	$La_{0.1}Ce_{0.1}Pr_{0.1}Gd_{0.1}Y_{0.1}Zr_{0.5}O_2$	LCPGY	High entropy
Reduced form (pyrochlore)	p-$Ce_2Zr_2O_7$	p-CeZrO	–
	p- $(La_{0.2}Ce_{0.2}Pr_{0.2}Gd_{0.2}Y_{0.2})_2Zr_2O_7$	p-LCPGY	High entropy
Re-oxidized form (kappa)	$κ$-$Ce_2Zr_2O_8$	$κ$-CeZrO	–
	$κ$-$(La_{0.2}Ce_{0.2}Pr_{0.2}Gd_{0.2}Y_{0.2})_2Zr_2O_{7+δ}$	$κ$-LCPGY	High entropy
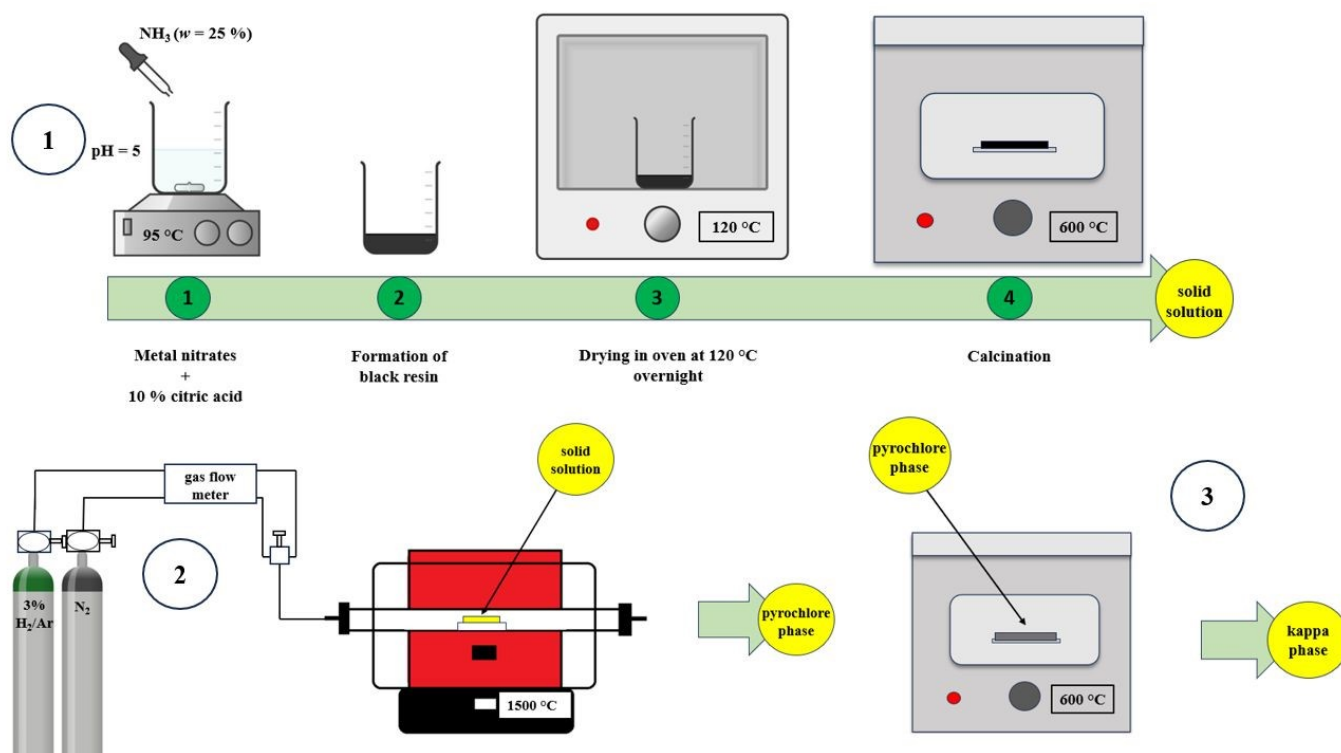
Scheme 1. Schematic representation of the step-by-step synthesis of ceria-zirconia systems; 1) schematic representation of the modified citrate-nitrate route; 2) reduction path of solid solution powders; 3) re-oxidation of pyrochlore phase powders to kappa phase.

Results and discussion

Structural and microstructural analysis.

Powder X-ray diffraction was performed to inspect the phase composition of the synthesized compounds. Using the FULLPROF software[49], PXRD patterns were further investigated with the Rietveld refinement. **Figure 1** and **Table 2** contain the Rietveld plots and refinement results of the synthesized solid solutions $Ce_{0.5}Zr_{0.5}O_2$ and $La_{0.1}Ce_{0.1}Pr_{0.1}Gd_{0.1}Y_{0.1}Zr_{0.5}O_2$, which are starting compounds for the preparation of pyrochlore (p)

and kappa (κ) phases. The refinement quality was evaluated by discrepancy factor, R_{wp}, and goodness-of-fit, $χ^2$. The observed (black), the difference (blue), and calculated (red) plots are shown, along with Bragg reflections (green) for the fit of the PXRD patterns. The average crystallite size values for prepared solid solutions powders were obtained by microstructural analysis and vary between 2 to 8 nm. The values of ionic radii play the main role in lattice parameters and cell volume which are very similar for both of tetragonal structures, but the average microstrain is higher for high entropy solid solution compound due to more than five elements in crystal lattice.
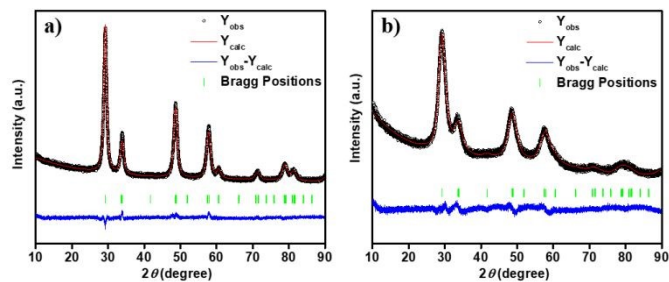
Figure 1. Rietveld plots of a) $Ce_{0.5}Zr_{0.5}O_2$ and b) $La_{0.1}Ce_{0.1}Pr_{0.1}Gd_{0.1}Y_{0.1}Zr_{0.5}O_2$.

Visualization of structures was performed using VESTA[50] software, as shown in **Figure S1**. According to Rietveld refinement results, both compounds crystallize in the tetragonal crystal system, space group $P4_2/nmc$. Their XRD patterns are similar, with slight peak shifts that indicate the difference in unit cell parameters is not disturbed due to doping with rare-earth elements. **Tables S2-S3** show additional structural parameters of starting solid solutions.

High-temperature reduction of solid solution powders reveals extremely sharp Bragg reflections for pyrochlore $Ce_2Zr_2O_7$ and pyrochlore-fluorite dual-phase $(La_{0.2}Ce_{0.2}Pr_{0.2}Gd_{0.2}Y_{0.2})_2Zr_2O_7$, respectively. The average crystallite size differs from 66 nm for $Ce_2Zr_2O_7$ to 69 and 87 nm for pyrochlore-flourite dual phase $(La_{0.2}Ce_{0.2}Pr_{0.2}Gd_{0.2}Y_{0.2})_2Zr_2O_7$. This indicates that, by reducing starting solid solution powders, the size of the unit cell expands due to the removal of oxide ions and compensating that with the increase in cation Ce and Pr size when changing the oxidation state from +4 (0.97 Å; 0.96 Å)[51] to +3 (1.14 Å; 1.13 Å)[51], respectively.

Figure 2 and **Table 3** show the Rietveld refinement results of the XRD patterns of the pyrochlore and kappa phases of both starting compounds. Reduced form of non-high entropy oxide consists of single-phase pyrochlore Fd–$3m$ structure, while the high-entropy form consists of two phases: fluorite Fm–$3m$ and pyrochlore Fd–$3m$. The pyrochlore structure can be seen as an ordered positioning of RE^{3+} (A site) and Zr^{4+} (B site) cations along the <110> direction. Here, Zr^{4+} ions have solid sixfold coordination by six identical Zr-O bonds[14,15]. An ordered pyrochlore Fd–$3m$ structure is characterised by the appearance of particular superstructure diffraction peaks applying CuKα radiation at the 2θ angles of 14° (111), 37° (331), 45° (511), and 51° (531), which are clearly visible in **Figure 2a** and **Figure 2c**. On the other hand, high-entropy form consists also of the fundamental fluorite Fm–$3m$ phase with space group 225, which is indicated by the peaks at (200), (220), and (311), which are very close to the ones of the pyrochlore phase. This behavior has already been investigated in other rare-earth pyrochlore zirconates. According to Wang et al.[22], the cation radius ratio r_A/r_B is 1.528 and the size disorder in p-$(La_{0.2}Ce_{0.2}Pr_{0.2}Gd_{0.2}Y_{0.2})_2Zr_2O_7$ is 4.96 %, which is less than 5%, meaning that the pyrochlore structure is favoured with this combination of lanthanide cations[52]. However, this combination involves Y^{3+} at A site which has a small eightfold coordination radius and favours the formation of the fluorite phase regardless of size disorder being less than 5%.

Chemical formula	$Ce_{0.5}Zr_{0.5}O_2$	$La_{0.1}Ce_{0.1}Pr_{0.1}Gd_{0.1}Y_{0.1}Zr_{0.5}O_2$
Crystal system	Tetragonal	
Space group	$P4_2/nmc$	
Z	2	
Unit cell parameters (Å)	a = 3.73 (2) c = 5.32 (1)	a = 3.73 (2) c = 5.32 (1)
Cell volume (Å³)	74.08	74.08
Calculated density (g/cm³)	6.58	6.46
Average crystallite size (nm)	7.31	2.82
Average microstrain (×10⁻⁴)	42.59	128.62
R_p, R_{wp}, R_e	11.0, 8.91, 7.36	12.6, 10.9, 7.94
χ^2	1.464	1.888

[2252]On top of that, it is also known that with the lowering of RE^{3+} radius, the intensity of the (200) fluorite phase peak gently increases, while the (400) peak symbolizing the pyrochlore phase progressively decreases[23]. Since the degree of disorder is still close to 5% and the combination of cations in our rare-earth zirconate includes yttrium, the formation of dual-phase fluorite-pyrochlore structures after reduction of the starting oxide $(La_{0.1}Ce_{0.1}Pr_{0.1}Gd_{0.1}Y_{0.1}Zr_{0.5}O_2)$ can be expected. **Figure 2c** shows a Rietveld refinement plot of XRD data belonging to p-$(La_{0.2}Ce_{0.2}Pr_{0.2}Gd_{0.2}Y_{0.2})_2Zr_2O_7$. At higher 2θ angles, peak splitting can be observed. This is the indicator of the existence of a dual phase: fluorite and pyrochlore. According to the Rietveld refinement results, there is 37.41 wt. % of pyrochlore and 62.59 wt. % of fluorite phase in the reduced form of high-entropy compound. For both reduced forms, non-high entropy and high entropy, the extracted structural parameters are shown in **Tables S4-S5**. As far as we know, there are no reports on the kappa form of high-entropy rare-earth zirconates ($HE_2Zr_2O_8$, HE = mixture of 5 equimolar metal cations) as opposed to non-high entropy zirconates. κ-$Ce_2Zr_2O_8$, which is well-known, crystallizes in the cubic crystal system, space group $P2_13$, with lower symmetry than the pyrochlore form, cubic Fd–$3m$. Unlike the pyrochlore phase, this structure is described by the ordered arrangement of RE^{4+} and Zr^{4+} ions. Here, Zr^{4+} has an eightfold coordination with eight non-equivalent Zr-O bonds that form two polyhedra. This finding explains the ability of high oxygen storage capacity (OSC) to release oxygen in kappa phases by using chemical reduction by hydrogen, two tetrahedra that can be formed with weaker Zr-O bonds. The transition between the pyrochlore and kappa form in ceria-zirconia-based oxides occurs because of the remarkable redox properties of $Ce^{3+/4+}$[14,15]. Since in p-$(La_{0.2}Ce_{0.2}Pr_{0.2}Gd_{0.2}Y_{0.2})_2Zr_2O_7$, La, Ce, Pr, Gd, and Y are all in +3 oxidation state, it is reasonable to expect

ARTICLE

them to form a pyrochlore structure. However, for kappa-structure to be formed, these cations have to be oxidized to the +4 state, and the only cations that undergo such a reaction are Ce^{3+} and Pr^{3+}. Thus, structurally we can propose the formation of two crystal structures of newly formed κ-$(La_{0.2}Ce_{0.2}Pr_{0.2}Gd_{0.2}Y_{0.2})_2Zr_2O_{7+\delta}$ after re-oxidation:

1) Partially oxidized pyrochlore phase (Fd–$3m$)
2) Partially oxidized kappa phase ($P2_13$)

Taking this into account, the Rietveld refinement was performed for both cases.

Kappa phase is formed when the 8b position in the pyrochlore Fd–$3m$ space group is fully filled, leading to distortion of Fd–$3m$ to $P2_13$ space group[14,15]. However, we expect 8b position to be only partially filled during re-oxidation

of p-$(La_{0.2}Ce_{0.2}Pr_{0.2}Gd_{0.2}Y_{0.2})_2Zr_2O_7$, so the question here is whether this amount is sufficient to distort the Fd–$3m$ space group. According to the Rietveld refinement results, a better fit was obtained taking into account the Fd–$3m$ space group, which would mean that the amount of incorporated oxygen (67,56 %) was not enough to distort Fd–$3m$ to the $P2_13$ space group. Also, there is no peak splitting at higher 2θ angles and lower value of goodness-of-fit, χ^2, which indicates the formation of single-phase partially oxidized pyrochlore κ-$(La_{0.2}Ce_{0.2}Pr_{0.2}Gd_{0.2}Y_{0.2})_2Zr_2O_{7+\delta}$ (**Figure 2d**). For kappa phases, the extracted structural parameters are presented in **Tables S6-S7**. Moreover, the Rietveld plot of κ-$(La_{0.2}Ce_{0.2}Pr_{0.2}Gd_{0.2}Y_{0.2})_2Zr_2O_{7+\delta}$, refined as partially oxidized kappa phase (cubic, space group $P2_13$) is shown in **Figure S2**.
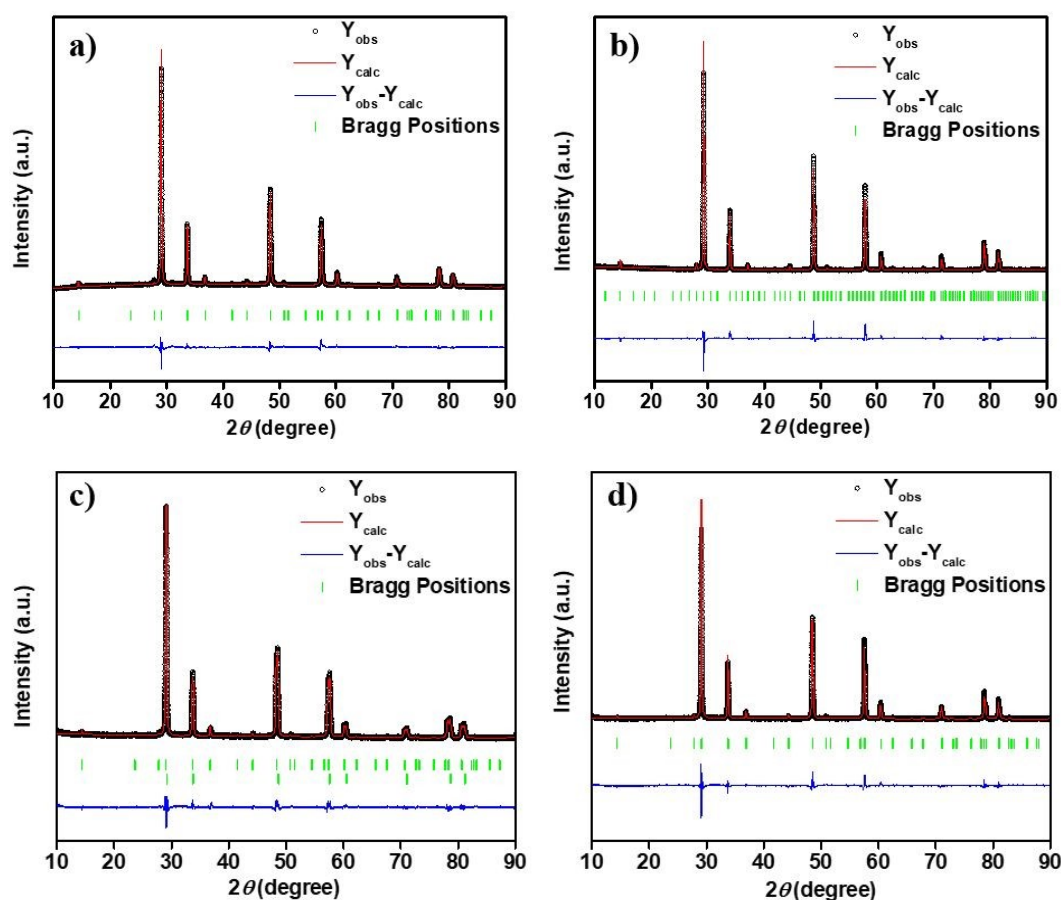

Figure 2. Rietveld plots of a) p-$Ce_2Zr_2O_7$, b) κ-$Ce_2Zr_2O_8$, c) p-$(La_{0.2}Ce_{0.2}Pr_{0.2}Gd_{0.2}Y_{0.2})_2Zr_2O_7$ and d) κ-$(La_{0.2}Ce_{0.2}Pr_{0.2}Gd_{0.2}Y_{0.2})_2Zr_2O_{7+\delta}$ (partially oxidized pyrochlore phase).

Raman spectroscopy was used to investigate the structure of the synthesized compounds further. **Figure 3** shows the Raman spectra of all synthesized compounds. The solid solution $Ce_{0.5}Zr_{0.5}O_2$ spectrum in **Figure 3a** clearly shows a typical Raman spectrum of a tetragonal solid solution[53]. There is a triply degenerate F_{2g} mode at 468 cm^{-1}, which is the only mode allowed for the cubic fluorite-structured ceria[54]. There is also a peak at 628 cm^{-1} that is often assigned to oxygen defects in cubic ceria[14,55]. However, the appearance of a mode at 305 cm^{-1} is a clear sign of a tetragonal symmetry breaking and therefore presents the distinction between cubic Fm–$3m$ and tetragonal $P4_2/nmc$ crystal structure[53]. Urban et al.[14] have already

explained this in their research. However, their solid solution is almost cubic since the additional peaks are present only as broad, low-intensity shoulders rather than defined peaks. The reason behind this could be a difference in the synthesis procedure for obtaining solid solution powder.

The high entropy solid solution $La_{0.1}Ce_{0.1}Pr_{0.1}Gd_{0.1}Y_{0.1}Zr_{0.5}O_2$ spectrum in **Figure 3b** displays a Raman spectrum similar to the one already reported for the high-entropy ceria-based compounds[47]. The sharp F_{2g} mode is almost invisible, and the defect band at 610 cm^{-1} dominates because of the addition of multiple elements in the fluorite structure of ceria. However, there is also a low-intensity broad shoulder at around 309 cm^{-1}

CrystEngComm

that might point toward symmetry breaking from cubic to the tetragonal crystal structure, similar to that reported by Urban et al[14,15].

The pyrochlore-type cubic Fd–3m crystal structure allows 6 Raman active modes $A_{1g} + E_g + 4F_{2g}$[54]. There are 4 Raman active modes visible at 258 cm^{-1}, 372 cm^{-1}, 414 cm^{-1}, and 590 cm^{-1} with shoulders at 220 cm^{-1} and 513 cm^{-1} in **Figure 3a**. This is in accordance with the spectral active modes calculated from the crystallographic information file (.cif), a method described by Kroumova et al[54].

Table 3. Results of the Rietveld refinement of p-Ce$_2$Zr$_2$O$_7$, κ-Ce$_2$Zr$_2$O$_8$, p-(La$_{0.2}$Ce$_{0.2}$Pr$_{0.2}$Gd$_{0.2}$Y$_{0.2}$)$_2$Zr$_2$O$_7$ and κ-(La$_{0.2}$Ce$_{0.2}$Pr$_{0.2}$Gd$_{0.2}$Y$_{0.2}$)$_2$Zr$_2$O$_{7+\delta}$.

Chemical formula	p-Ce$_2$Zr$_2$O$_7$	κ-Ce$_2$Zr$_2$O$_8$	p-(La$_{0.2}$Ce$_{0.2}$Pr$_{0.2}$Gd$_{0.2}$Y$_{0.2}$)$_2$Zr$_2$O$_7$		κ-(La$_{0.2}$Ce$_{0.2}$Pr$_{0.2}$Gd$_{0.2}$Y$_{0.2}$)$_2$Zr$_2$O$_{7+\delta}$ partially oxidized pyrochlore phase	κ-(La$_{0.2}$Ce$_{0.2}$Pr$_{0.2}$Gd$_{0.2}$Y$_{0.2}$)$_2$Zr$_2$O$_{7+\delta}$ partially oxidized kappa phase
Crystal system	Cubic					
Space group	Fd–3m	$P2_13$	Fd–3m	Fm–3m	Fd–3m	$P2_13$
Z	8	1	8		8	1
Unit cell parameters (Å)	a = 10.64 (9)	a = 10.56 (1)	a = 10.65 (9)	5.3 (2)	a = 10.62 (9)	a = 10.62 (1)
Cell volume (Å^3)	1205.42(8)	1178.38	1209.19 (8)	148.99(7)	1196.45(8)	1196.86(8)
Calculated density (g/cm^3)	6.33	6.66	15.38	7.04	6.36	15.74
Phase content (wt. %)	100	100	37.41	62.59	100	100
Average crystallite size (nm)	66.1(3)	82.9	69.4(5)	87.4(3)	64.3(5)	62.3(7)
Average microstrain (×10^{-4})	11.24(9)	4.23	13.1(1)	10.2(3)	4.47(4)	4.23(1)
R_p, R_{wp}, R_e	18.2, 12.9, 5.58	19.5, 14.2, 5.94	17.1, 11.1, 4.52		22.6, 16.2, 5.81	24.1, 17.2, 6.12
χ^2	5.38	5.71	6.05		7.76	7.94

In **Figure 3b**, there are also 4 Raman active modes at 301 cm^{-1}, 385 cm^{-1}, 511 cm^{-1}, and 600 cm^{-1} with a low-intensity shoulder at around 220 cm^{-1}. These modes are similar to the (La$_{0.2}$Nd$_{0.2}$Sm$_{0.2}$Eu$_{0.2}$Gd$_{0.2}$)$_2$Zr$_2$O$_7$ modes, recently studied by Luo et al[56]. Both pyrochlore phases in **Figure 3** have broad Raman modes. The broadening of Raman modes occurs due to the disorder in the oxygen sublattice[52]. This could arise from the fact that oxygen position 8b in the structure of p-Ce$_2$Zr$_2$O$_7$ is empty[15]. In p-(La$_{0.2}$Ce$_{0.2}$Pr$_{0.2}$Gd$_{0.2}$Y$_{0.2}$)$_2$Zr$_2$O$_7$, there is an additional structural disorder in the cationic sublattice introduced by the incorporation of multiple cations, which also impacts the A–O and B–O bond lengths[56].

The kappa phase, i.e. cubic $P2_13$ structure, contains 144 Raman active modes, $24A + 24E_1 + 24E_2 + 72F$[54]. Many of them are not visible in **Figure 3,** and it is difficult to resolve all of them[14]. Peaks in **Figure 3a** are narrow in frequency, which is probably due to the large unit cell, which contains only a few different atomic species[14]. However, the Raman spectrum of the kappa phase in **Figure 3b** resembles the pyrochlore phase in the same figure. There are broad peaks at 296 cm^{-1}, 394 cm^{-1}, and 602 cm^{-1} and shoulder peaks at 225 cm^{-1} and 525 cm^{-1}. The reason

behind this could be that oxygen position 8b is only partially occupied when Ce^{3+} and Pr^{3+} are oxidized to Ce^{4+} and Pr^{4+}, respectively. Therefore, the disorder in the oxygen sublattice is preserved both due to the partially empty 8b position and the remaining disorder in the cationic sublattice. This would confirm the hypothesis that κ-(La$_{0.2}$Ce$_{0.2}$Pr$_{0.2}$Gd$_{0.2}$Y$_{0.2}$)$_2$Zr$_2$O$_8$ is actually a partially oxidized pyrochlore compound (La$_{0.2}$Ce$_{0.2}$Pr$_{0.2}$Gd$_{0.2}$Y$_{0.2}$)$_2$Zr$_2$O$_{7+\delta}$.

The summary of observed Raman active modes for pyrochlore and kappa phases can be found in **Table S8**.

Raman spectroscopy can also be used to distinguish between Ce^{3+} and Ce^{4+} compounds because Ce^{3+} shows a characteristic scattering peak at around 2100 cm^{-1} [57,58]. This scattering peak represents $^2F_{5/2}$–$^2F_{7/2}$ transitions[59] for Ce^{3+} and it usually occurs when Ce^{3+} is present in the structure of a compound, such as Ce$_2$O$_3$ or pyrochlore Ce$_2$Zr$_2$O$_7$[60,61]. However, this peak is not detected if surface Ce^{3+} makes no structural change (such as reduction of CeO$_2$ to Ce$_2$O$_3$)[60,62]. Surface defects are usually detected by defect bands, for example, in CeO$_2$, they are present from 500 to 700 cm^{-1} [62].
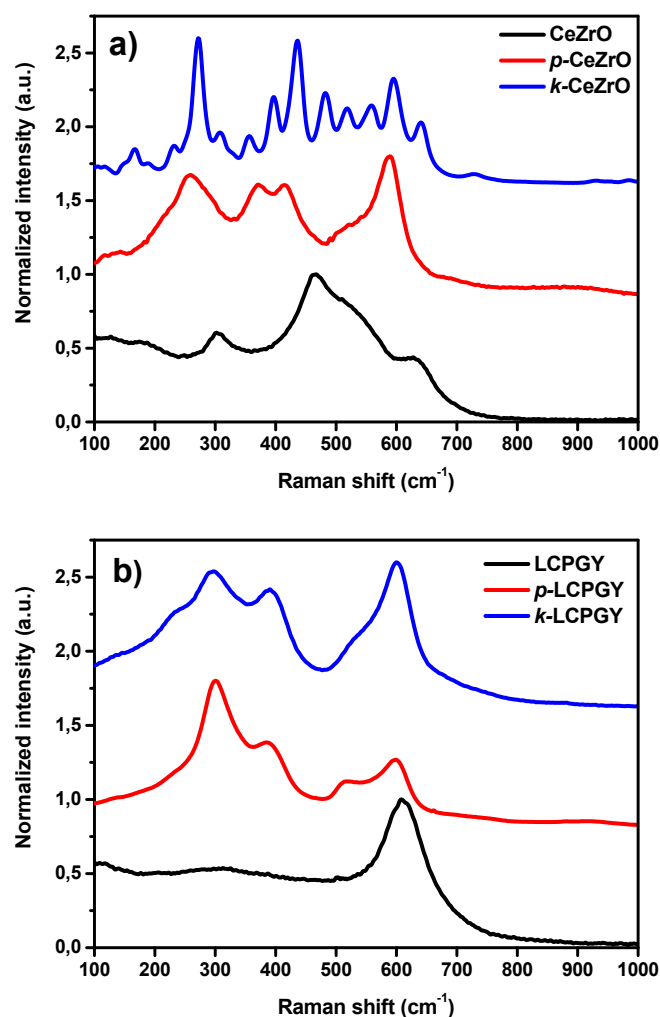
Figure 3. Raman spectra of a) $Ce_{0.5}Zr_{0.5}O_2$ (black), p-$Ce_2Zr_2O_7$ (red) and κ-$Ce_2Zr_2O_8$ (blue) and b) $La_{0.1}Ce_{0.1}Pr_{0.1}Gd_{0.1}Y_{0.1}Zr_{0.5}O_2$ (black), p-$(La_{0.2}Ce_{0.2}Pr_{0.2}Gd_{0.2}Y_{0.2})_2Zr_2O_7$ (red) and κ-$(La_{0.2}Ce_{0.2}Pr_{0.2}Gd_{0.2}Y_{0.2})_2Zr_2O_{7+\delta}$ (blue).

Figure S3 depicts the area between 2000 cm^{-1} and 2300 cm^{-1} in Raman spectra of both compounds in their solid solution, pyrochlore and kappa form. Only the pyrochlore form shows a scattering signal, at 2157 cm^{-1} for p-$Ce_2Zr_2O_7$ and at 2123 cm^{-1} for p-$(La_{0.2}Ce_{0.2}Pr_{0.2}Gd_{0.2}Y_{0.2})_2Zr_2O_7$. This means that only pyrochlore-type compounds are Ce^{3+}-based.

XPS was used to investigate the surface of the synthesized catalysts. The high-resolution C 1s spectra with four deconvoluted peaks for C-C/C-H, C-O, COO/COOH, and carbonate are visible in **Figure S4.** Three peaks (C-C/C-H, C-O, COO/COOH) probably originate from carbonateous species adsorbed on the surface of the material after preparation and during the sample transfer to the XPS spectrometer[63–65]. Rare-earth-based oxides tend to adsorb carbon dioxide when exposed to air and form carbonate species on the surface[66–69], which is why the carbonate peak is detected. The high-resolution O 1s spectra in **Figure 4** for all samples show peaks corresponding to lattice oxygen (labelled O_L), surface-adsorbed oxygen species (O_{ads})[70], adsorbed water, and oxidized

adventitious carbonaceous species[71]. For CeZrO, LCPGY, p-LCPGY, and κ-LCPGY, probably some water remained on the surface (peak designated in **Figure 4**). By comparing the surface atomic concentrations of O_{ads} for CeZrO catalysts, the highest surface concentration of O_{ads} relative to surface atomic concentration of all O-containing species, i.e O_{total}, was found for p-CeZrO ($O_{ads}/O_{total} = 0.294$), while CeZrO ($O_{ads}/O_{total} = 0.063$) and κ-CeZrO ($O_{ads}/O_{total} = 0.114$) phases have significantly lower amounts than p-CeZrO. This is due to anion-deficient distorted fluorite structure of p-CeZrO with 1/8 of empty tetrahedral anionic position, known as oxygen vacancies, since O_L decreases significantly compared to ordered structures of t-CeZrO and κ-CeZrO phases. On the other hand, p-LCPGY has a slightly lower O_{ads}/O_{total} of 0.149 compared with p-CeZrO ($O_{ads}/O_{total} = 0.294$), due to phase duality, since it consists of both pyrochlore and fluorite phases. However, this ratio is similar for LCPGY ($O_{ads}/O_{total} = 0.187$) and κ-LCPGY ($O_{ads}/O_{total} = 0.180$). **Tables S9-S11** show the relative surface atomic concentration ratios of O_{ads}/O_{total}, Ce^{3+}/Ce^{4+}, and Pr^{3+}/Pr_{total} evaluated from the deconvoluted peaks. To calculate the amount of Ce^{3+}, the fitted intensity of the v and u features was adapted. The peaks v, v'', v''', u, u'', and u''' correspond to cerium ions in the oxidation state +4, while v^0, v', u^0, and u' are assigned to Ce^{3+} ions[48,72–74]. The high-resolution Ce 3d XPS spectra in **Figure 5** show that the Ce^{3+}/Ce^{4+} ratio in CeZrO compounds follows the trend kappa (0.32) < starting oxide (0.37) < pyrochlore (0.48). This is expected because the pyrochlore phase is the reduced form and therefore should contain the highest amount of Ce^{3+}. The starting oxide has a significantly smaller crystallite size (around 7 nm) compared to the kappa phase (83 nm), resulting from sintering at high temperatures after reduction and re-oxidation. This is why starting oxide also has more defects, i.e. oxygen vacancies, which are directly correlated to Ce^{3+} content. This is the reason for the larger amount of Ce^{3+} in the starting oxide compared to the kappa phase.

Deconvoluted high-resolution Ce 3d XPS spectra for high-entropy LCGPY compounds are shown in **Figure 6**. High-entropy LCPGY compounds do not follow the same trend. In these compounds, the Ce^{3+}/Ce^{4+} ratio decreases in the following order: pyrochlore (0.30) < kappa (0.51) < starting oxide (0.54). This is unusual behaviour since pyrochlore, as a reduced phase, should contain the highest amount of Ce^{3+}. The reason for this could be in the dual-phase problem. According to Rietveld refinement, approximately 37 wt.% of the pyrochlore phase is present in p-LCPGY, while the rest is fluorite. Fluorite ceria-based structures can be reduced, but they are also easily re-oxidized under ambient conditions after exposure to air, especially at the surface of RE-doped forms[75]. Fluorite phase in p-LCPGY has a significantly larger crystallite size (87 nm) compared to the starting fluorite oxide (around 3 nm). It also possesses a higher degree of crystallinity, which is inversely proportional to the concentration of defects, i.e. oxygen vacancies, and consequently, the concentration of Ce^{3+} ions. Further re-oxidation of the pyrochlore dual-phase compound leads to the formation of a single-phase partially oxidized pyrochlore structure.
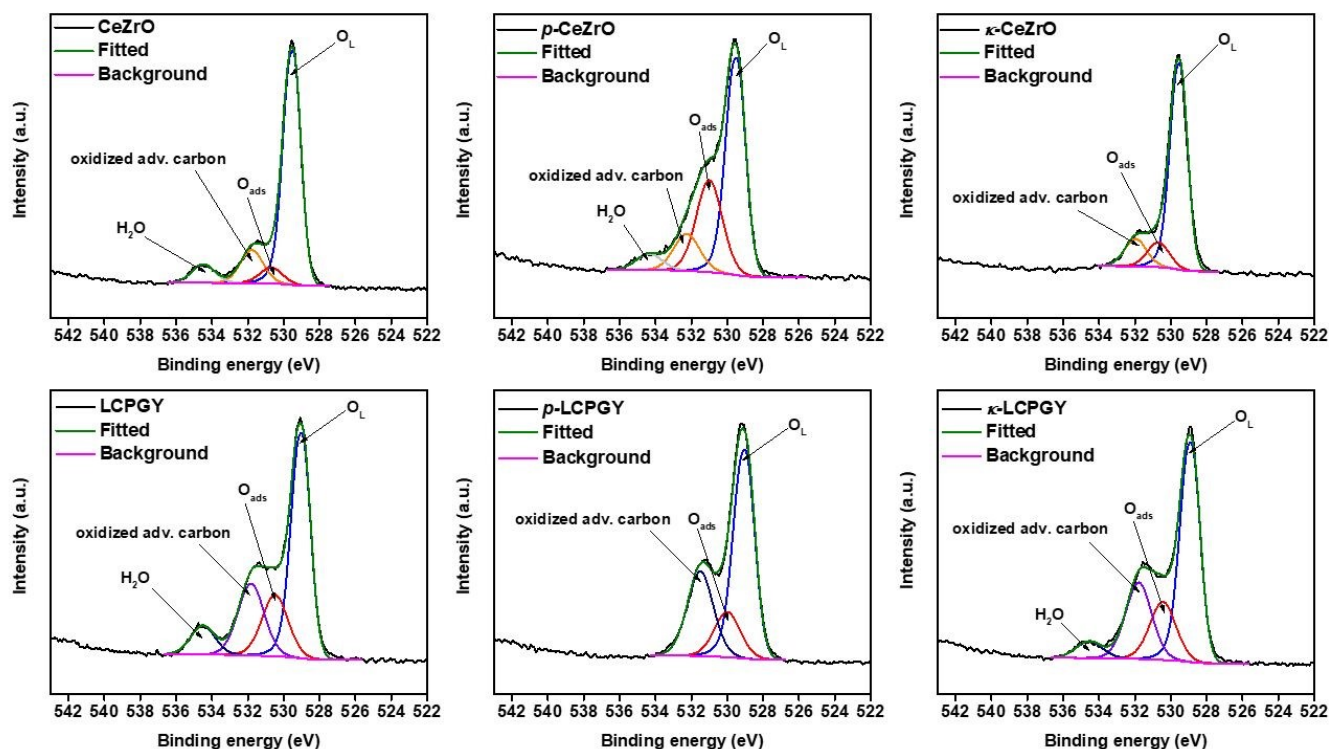
ARTICLE

Figure 4. Deconvoluted high-resolution O 1s XPS spectra of CeZrO, LCPGY, *p*-CeZrO, *p*-LCPGY, *κ*-CeZrO and *κ*-LCPGY.

Figure S5 shows high-resolution Pr 3d XPS spectra for the high-entropy LCPGY compounds. The Pr environment is similar for all the compounds. It was shown previously[76] that the high-resolution XPS spectra for Pr_2O_3 do not exhibit the doublet for a"/b"; thus, it can be concluded that this doublet belongs only to Pr^{4+} ions[76]. On the other hand, doublets for a/b and a'/b' are both present in PrO_2 and Pr_2O_3, so they can't be assigned to a specific oxidation state. To estimate the amount of Pr^{3+} ions, a formula proposed by Sinev et al.[77] was used, which takes into account the peak ratio of a"/a' to calculate and estimate the surface concentration of a particular oxidation state of praseodymium ions. In this case, the highest surface concentration of Pr^{3+} has pyrochlore LCPGY, which corresponds to previous reports[78–80] since it is the only reduced form of starting oxide, LCPGY, where Pr^{4+} is present, and the same in *κ*-LCPGY.

The high-resolution Zr 3d XPS spectra for all the compounds (**Figure S6**) show $Zr3d_{5/2}$ and $Zr3d_{3/2}$ doublets, which correspond to ZrO_2. LCPGY shows an additional doublet, probably corresponding to sub-oxides[81,82].

High-resolution XPS spectra for La 3d, Gd, and Y are shown in **Figures S7-S9**. Y 3d spectrum was deconvoluted using constraints reported previously[83,84]. It consists of a doublet corresponding to Y $3d_{3/2}$ (at around 159 eV) and Y $3d_{5/2}$ (at around 157 eV). For LCPGY and *κ*-LCPGY, an additional Si 2s peak appears, which most likely originates from the carbon tape.

The deconvolution of the high-resolution La 3d, Gd 3d and Gd 4d XPS spectra is challenging due to the existence of charge-transfer satellites[85,86], so they are only visualized in **Figures S7 and S8** showing La $3d_{3/2}$ (at around 855 eV) and La $3d_{5/2}$ (at 833 eV), Gd $3d_{3/2}$ (at around 1219 eV) and Gd $3d_{5/2}$ (at around 1187 eV); Gd $4d_{3/2}$ (at around 148 eV) and Gd $4d_{5/2}$ (at around 143 eV), which is consistent with previously reported results[67,68,87–89]. The magnitude of multiplet splitting in La 3d spectra of LCPGY, *p*-LCPGY, and *κ*-LCPGY is in the range of 4.8–5.0 eV, corresponding to lanthanum oxide[67,85].

The morphology of all synthesized compounds was inspected using scanning electron microscopy. SEM images are shown in **Figure 7a-f. Figures 7a** and **7d** show SEM images of the starting oxides, respectively. Since the calcination temperature used for their synthesis was only 600 °C, they appear to have smaller

grain sizes than their reduced (**Figures 7b and 7e**) and re-oxidized (**Figures 7c and 7f**) counterparts. Also, they seem to be porous. Reduced and re-oxidized forms of starting oxides consist of larger grains, which is expected taking into account that they were additionally calcined at 1500 °C and 600 °C, respectively. This behaviour is expected due to sintering[90]. However, high-entropy forms of reduced and re-oxidized compounds seem to form a porous network. This could affect the increase of specific surface area, thus making them more efficient as catalysts.

Also, compared to the average crystallite size in **Table 3**, the average grain size shown in **Figure 7** is much larger. The reason behind this is that grains can contain one or multiple crystallites. Polycrystalline materials usually contain multiple crystallites inside larger grains, especially due to sintering at high temperatures[42,44–46,90,91]. **Figure S10** shows these SEM images at low magnification where it is clear that these compounds are mostly porous sheet-like powders consisting of smaller grains. **Figure S11** shows SEM image of LCPGY where it is visible that it consists of both smooth and porpous surfaces. Smooth surfaces are present probably due to sintering[90,91]. [90,91]
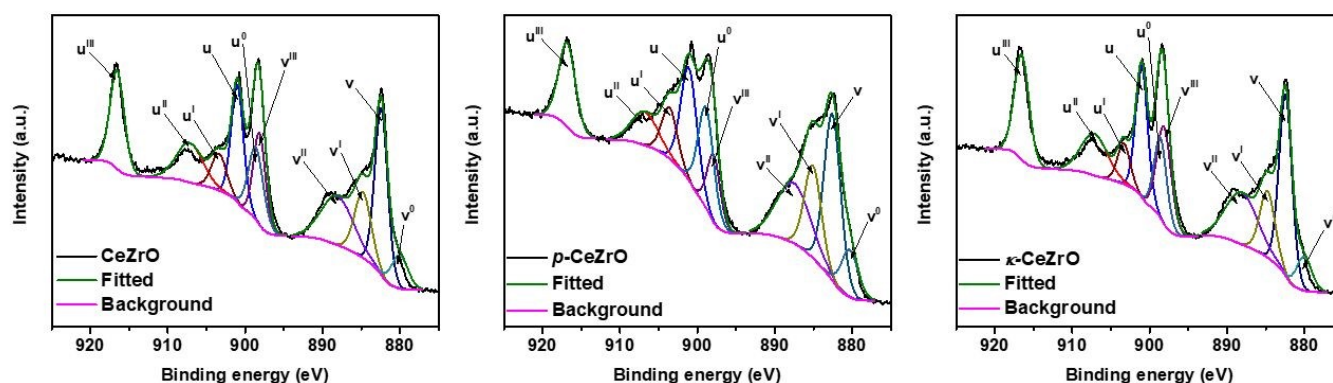

Figure 5. Deconvoluted high-resolution Ce 3d XPS spectra of CeZrO, *p*-CeZrO, and *κ*-CeZrO.

Chemical content was investigated by energy-dispersive X-ray spectroscopy. When calculating the empirical formula, the oxygen content was normalized to 2 for the solid solutions ($Ce_{0.5}Zr_{0.5}O_2$ and $La_{0.1}Ce_{0.1}Pr_{0.1}Gd_{0.1}Y_{0.1}Zr_{0.5}O_2$), to 7 for the pyrochlore phases ($Ce_2Zr_2O_7$ and $(La_{0.2}Ce_{0.2}Pr_{0.2}Gd_{0.2}Y_{0.2})_2Zr_2O_7$), and to 8 for the kappa phases ($Ce_2Zr_2O_8$ and $(La_{0.2}Ce_{0.2}Pr_{0.2}Gd_{0.2}Y_{0.2})_2Zr_2O_8$). There are visible deviations from

the desired chemical composition, but EDS quantification is not very precise, so these deviations are allowed. The summary of EDS quantitative analysis of solid solutions, pyrochlore, and kappa phases can be found in **Tables S12** and **S13**. Elemental mapping was also performed for kappa forms of synthesized compounds, and elemental maps are shown in **Figures S12** and **S13**.
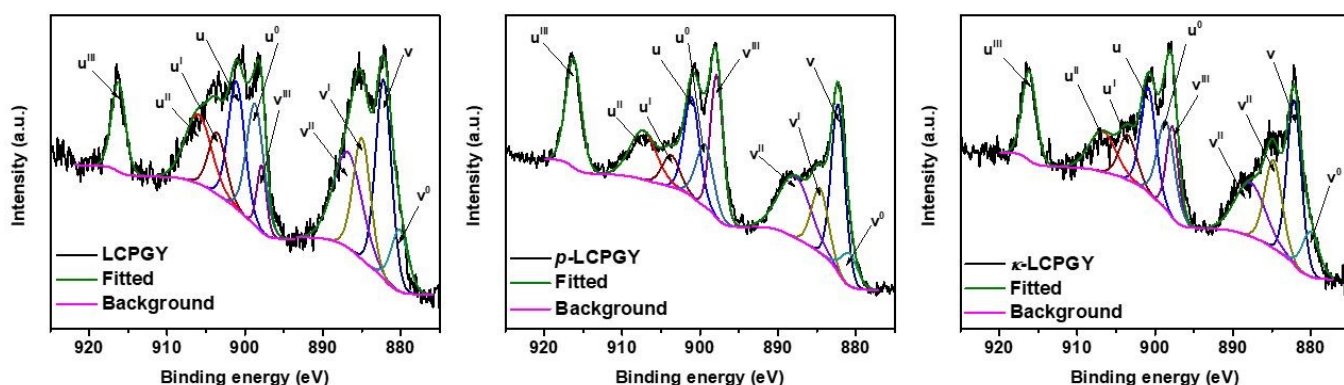

Figure 6. Deconvoluted high-resolution Ce 3d XPS spectra of LCPGY, *p*-LCPGY, and *κ*-LCPGY.

In case of *κ*-$Ce_2Zr_2O_8$, the distribution of involved elements (Ce, Zr, O) is homogeneous.
On the other hand, elemental maps of its high-entropy counterpart, *κ*-$(La_{0.2}Ce_{0.2}Pr_{0.2}Gd_{0.2}Y_{0.2})_2Zr_2O_{7+δ}$, show that while the distribution of Ce, Pr, La, and Gd is uniform, Zr and Y seem to have a somewhat different distribution, different from Ce, Pr, La, and Gd, but similar to each other.

For all powder samples, nitrogen adsorption-desorption isotherms (**Figure S14**) were accomplished at a temperature of −196 °C using Autosorb IQ (Quantachrome Instruments USA), a surface gas sorption analyzer. Solid solution and high-entropy solid solution adsorption isotherms belong to the group of isotherm type IV, which are characteristic of mesoporous materials. In contrast, pyrochlore and kappa compounds have quite different isotherm shapes and very small adsorbed

CrystEngComm

volumes. This can be explained by the high reduction temperatures of solid solutions to obtain pyrochlore phases (1500 °C) since the crystallite size has remarkably increased. These types of problems can occur due to the cavitation effect or pore blocking[92]. Kappa phase is an oxidized pyrochlore phase, so the assumption is the same.
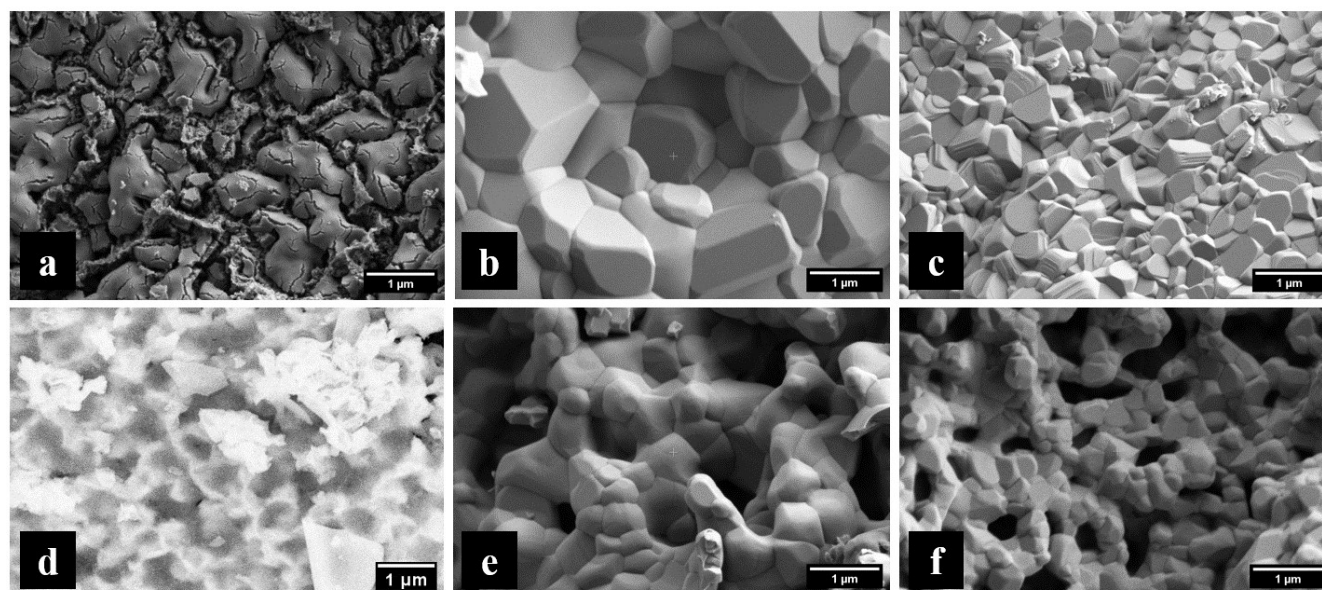
Figure 7. SEM images of a) CeZrO, b) *p*-CeZrO, c) *κ*-CeZrO, d) LCPGY, e) *p*-LCPGY, and f) *κ*-LCPGY.

Using the Brunauer–Emmett–Teller (BET) and the nitrogen adsorption isotherm data, the specific surface areas of the obtained mesoporous materials were calculated[93,94]. The highest values showed starting solid solutions $Ce_{0.5}Zr_{0.5}O_2$ and its high-entropy counterpart $La_{0.1}Ce_{0.1}Pr_{0.1}Gd_{0.1}Y_{0.1}Zr_{0.5}O_2$ of 57.55 m^2/g and 36.73 m^2/g, respectively. The specific surface area of these oxides can vary from 30 to 400 m^2/g, depending on which synthesis method has been used. For example, Dao and Luu[95] used the combustion method to prepare nanostructured $Ce_{0.5}Zr_{0.5}O_2$ using polyvinyl alcohol at 600 °C and obtained a value of 73 m^2/g[95]. On the other hand, Hadi et al.[96] prepared $CeZrO_2$ nanoparticles using the water/oil microemulsion method at room temperature with and without the calcination process. The results showed that nanoparticles synthesized without calcination have a size under 10 nm and a high specific surface area of around 170 m^2/g. On the contrary, using the calcination process, the particle size increased, and the specific surface area dropped to around 47 m^2/g[96]. Comparing BET specific surface areas of pyrochlore and kappa phases of both types of compounds, high-entropy powders show greater values, which are proportional to their catalytic efficiency towards methane oxidation. Although a high-entropy solid solution has a higher specific surface area and pore volume than its oxidized kappa form, it can be assumed that high oxygen storage capacity improves catalytic activity. Pore sizes were calculated using the Barrett-Joyner-Halenda (BJH) test method[97]. Based on the appearance of the isotherm and the obtained data on the pore size of 3-5nm, it can be presumed that these powders are mesoporous materials (2-50 nm)[98]. Total pore volume was obtained from the amount of nitrogen adsorbed at the relative pressure (p/p_0) of 0.99 and shows

superior advantages to starting solid solutions, which is to be expected due to the highest specific surface area. **Table 4** shows values of specific surface area, pore size, and total pore volume of synthesized non-high entropy and high-entropy catalysts.

Table 4. BET specific surface area, pore volume, and pore size of synthesized powders.

POWDER	BET specific surface area ($m^2\ g^{-1}$)	Pore volume ($cm^3\ g^{-1}$)	Pore size (nm)
t-CeZrO	57.553	0.131	3.4
p-CeZrO	10.275	0.007	4.9
κ-CeZrO	5.289	0.006	3.1
t-LCPGY	36.731	0.107	3.4
p-LCPGY	16.810	0.015	3.1
κ-LCPGY	21.510	0.016	3.4

Oxygen uptake analysis.

Thermogravimetric analyses were conducted in the oxidative (O_2) and inert (argon) atmospheres. **Figure 8** shows the mass changes of the synthesized pyrochlore forms as a function of temperature. Mass change in the oxidative atmosphere can correspond to unit cell expansion or oxygen uptake due to oxidation[99,100]. Here, we observe a slight increase in the mass value (up to 0.3 %) in an inert atmosphere that can be attributed to unit cell expansion.
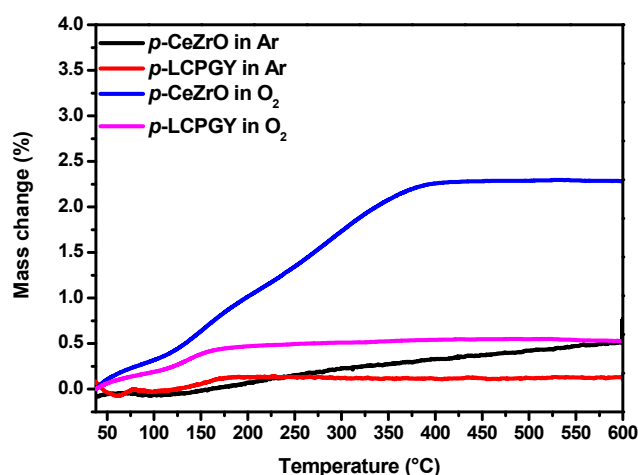
ARTICLE

Figure 8. Mass change as a function of temperature for reduced forms of starting oxides (*p*-CeZrO and *p*-LCPGY) in oxidative (O$_2$) and inert (Ar) atmosphere.

[99,100]However, there is a much larger mass increase in the non-high-entropy form (*p*-Ce$_2$Zr$_2$O$_7$) in the oxidative atmosphere, up to 2.2 % which can be the result of oxidation of Ce^{3+} to Ce^{4+}, i.e. oxygen uptake. This is similar to previous findings[14,15]. Oxygen uptake here results in the phase transition from pyrochlore to the kappa phase. As for the high-entropy form, there is only a slight increase in mass (0.5 %) since there is only 0.2 mol of Ce^{3+} and Pr^{3+} in the compound, while other cations cannot be oxidized. Integrated mass change as a function of temperature is shown in **Figure 9**.
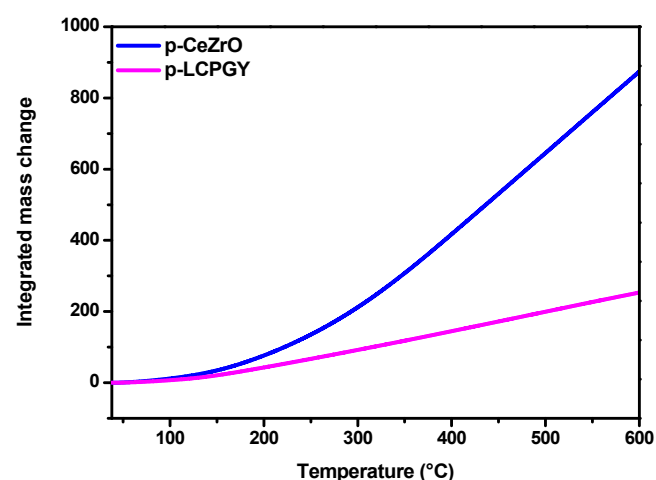

Figure 9. Integrated mass change as a function of temperature for reduced forms (*p*-CeZrO and *p*-LCPGY) of starting oxides in oxygen atmosphere.

Mass change occurs rapidly and at lower temperatures in the non-high-entropy form of a reduced oxide (*p*-CeZrO) than in its high-entropy counterpart (*p*-LCPGY).

Temperature-programmed desorption.

Temperature-programmed desorption (TPD) was conducted in the CH$_4$/Ar atmosphere using thermogravimetric analysis (TGA) for the increase in temperature and quadrupole mass

spectrometry (QMS) for the detection of gasseous products. Methane oxidation can be written using **Equation (2)**:

$$CH_4(g) + 2O_2(g) \rightarrow CO_2(g) + 2H_2O(g) \qquad (2)$$
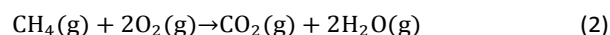
If methane reacts with the oxygen-rich surface of the catalyst, it is oxidized to carbon dioxide, and water (vapor) is formed. However, for this reaction to occur, energy is needed, which is why it takes place at higher temperatures. According to the QMS (**Figure S15**), the only products that were detected were carbon dioxide and water, which means that the surfaces of the prepared compounds were sufficiently oxygen-rich to induce a complete oxidation of methane. **Figure 10a-b** shows the ion current change of carbon dioxide as a function of temperature. The methane oxidation for all used catalysts takes place at around 400 °C where adsorption of methane occurs, followed by carbon dioxide desorption. Ion current change increases proportionally with the increase in desorbed carbon dioxide. As seen from **Figure 10b**, high-entropy forms of starting oxide and its re-oxidized counterpart have the largest amount of ion current change. This means that they produce larger amounts of carbon dioxide than other forms of oxides, probably because of the larger amount of oxygen at the surface i.e. larger oxygen storage capacity (OSC).

Integrated ion current change (**Figure 11**) shows CO$_2$ desorption as a function of temperature and time. High-entropy forms of the starting and re-oxidized compounds show the highest CO$_2$ desorption rate (the largest slope), which starts slightly before 400 °C. This makes them more effective in methane oxidation. Also, the same trend can be observed in **Figure 9b**, where it is evident that CO$_2$ formation occurs rapidly at the surface of the starting solid solution and the re-oxidized form of high-entropy compounds. After approximately 100 minutes (around 1.7 h), the production of CO$_2$ is terminated.

Since the catalysts we presented here are metal oxides, it is generally considered that they catalyse the oxidation of methane via Mars-van Krevelen mechanism[101] which follows 3 steps:

1) Initiation where activation and dissociation of methane on the surface of catalyst occurs;

2) Redox cycle where surface oxygen species react with the adsorbed methane and oxidizes it while the catalyst reduces itself;

3) Formation of products where they are desorbed from the catalyst surface (such as carbon dioxide and water when total oxidation occurs). In this mechanism, the rate-determining step is the activation of the first C-H bond in methane[102,103]. This is why the external heating is required to overcome this barrier.
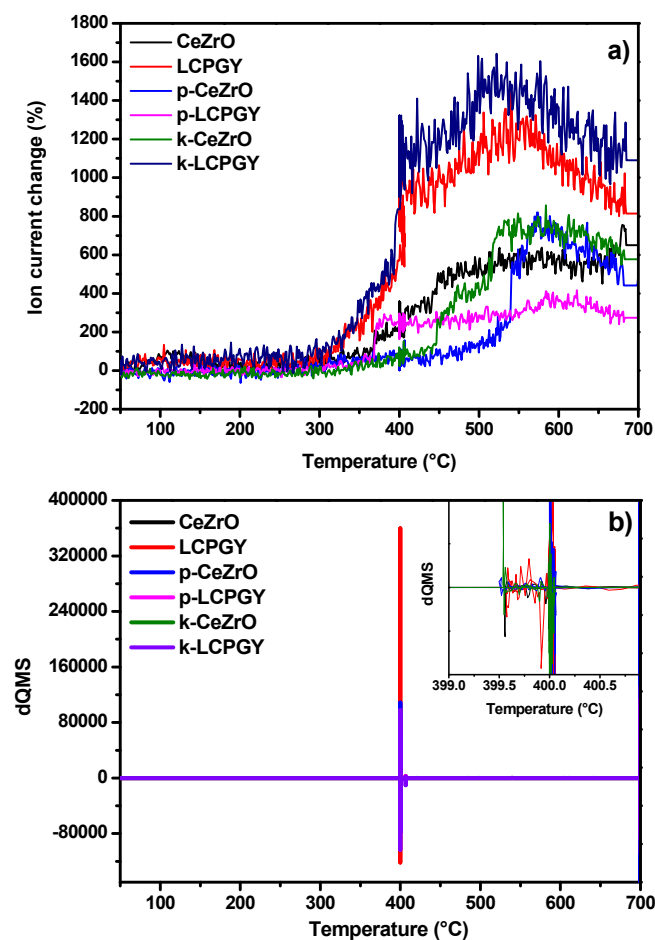
Figure 10. a) Ion current change and b) Derivation of ion current change as a function of temperature during the exposure of CeZrO, LCPGY, *p*-CeZrO, *p*-LCPGY, *κ*-CeZrO, and *κ*-LCPGY to methane flow (100 mL/min).

Most of the catalysts operate at temperatures of 500 °C or higher, and the aim over the years was to reduce the energy input[104–106]. According to literature[102,106], catalysts that operate at temperatures below 500 °C are considered low-temperature operating catalysts. The catalysts we present in this paper have started the oxidation process around 400 °C. The maximum of ion current change for every synthesized compound occurs at different temperatures and is presented in **Figure 12a**. These values represent the largest amount of detected carbon dioxide after the oxidation of methane. The most effective compound is *κ*-LCPGY, followed by LCPGY. The largest amount of detected carbon dioxide is in the range 520 –540 °C for these compounds. CeZrO produces the largest amount of carbon dioxide at around 680 °C, which is the highest operating temperature of all six compounds.   The maximum of ion current change (**Figure 10a**) is around 500 °C. However, they could still be considered as low-temperature catalysts because C-H bond activation still occurs around 400 °C. **Figure 10b** shows the ion current change (detected amount of carbon dioxide) at the beginning of the oxidation process (400 °C). Even if a catalyst possesses a large activity, its stability is also important. If the catalyst is still stable after the catalytic reaction, it can be reused in the same reaction. Therefore, XRD patterns of the catalysts after

exposure to methane flow were inspected to investigate the stability of the used catalysts.

Solid solution CeZrO clearly decomposes after the temperature-programmed desorption, while its high-entropy form (LCPGY) remains unchanged primarily (**Figure S16**). LCPGY only shows sharper peaks as a result of additional sintering during the methane oxidation process (up to 700 °C). However, since pyrochlore and kappa forms could generally undergo structural changes due to oxidation and reduction, we have inspected these XRD patterns more closely, using Rietveld refinement (**Figures S17-S20**). Rietveld refinement results are summarized in **Table S14**.
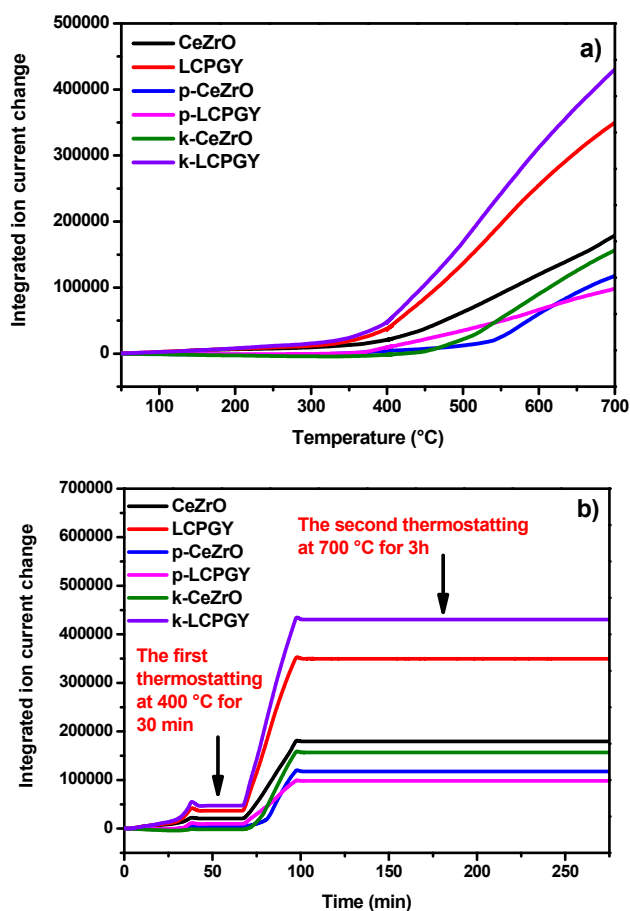

Figure 11. Integrated ion current change as a function of temperature (a) and time (b) of CeZrO, LCPGY, *p*-CeZrO, *p*-LCPGY, *κ*-CeZrO, and *κ*-LCPGY.

According to the refinement results, *p*-CeZrO undergoes partial phase transition from pyrochlore *Fd*–3*m* to fluorite *Fm*–3*m*. Thus, it is finally a dual-phase compound consisting of both pyrochlore (34.16 w.t. %) and fluorite forms (65.84 w.t. %), which can also be observed from peak splitting at higher 2*θ* angles. A similar thing occurs with its kappa form, *κ*-CeZrO. Peak splitting at higher 2*θ* angles revealed phase duality and the co-existence of fluorite *Fm*–3*m* structure. Since these catalysts oxidize methane, they should undergo a reduction process. Thus, we assumed that the kappa form could undergo a phase transition from kappa *P*2₁3 to pyrochlore *Fd*–3*m* structure. However, a better fit was obtained for the kappa *P*2₁3 structure. As a result, *κ*-CeZrO also shows phase duality after the methane

ARTICLE

oxidation reaction, consisting of kappa $P2_13$ (65 w.t.%) and fluorite $Fm–3m$ (35 w.t.%) structure due to partial phase transition.

On the contrary, p-LCPGY, which consisted of pyrochlore (37 w.t. %) and fluorite structures (63 w.t.%) before the methane oxidation, is now a single-phase pyrochlore $Fd–3m$ compound. This phase transition probably occurred due to additional reduction of the compound during methane oxidation.

The only compound besides LCPGY that remained structurally unchanged after the methane oxidation was κ-LCPGY (partially oxidized pyrochlore $Fd–3m$, with the same amount of incorporated oxygen (68 %) at the 8b position, making it reusable and efficient in catalytic oxidation reactions, such as methane oxidation.

Guided by Rietveld refinement results, high-entropy forms show a surprising shift towards stability and single-phase structures. Comparing non-high entropy and high-entropy pyrochlore forms after temperature programmed-deposition (methane oxidation), it can be seen that doping A sites with multiple rare-earth elements gives structure stability and therefore superior catalytic activity.

Figure 12. Ion current change at 400 °C (a) and maximum of ion current change versus temperature (b) of CeZrO, LCPGY, p-CeZrO, p-LCPGY, κ-CeZrO, and κ-LCPGY.

Besides methane oxidation, these compounds could be used in other oxidation reactions, such as the oxidation of carbon monoxide or volatile organic compounds (VOCs)[107–109], but also in electrochemical water splitting reactions[110–119]. These redox reactions could also be light- or temperature-assisted[98,120,121].

Conclusions

To sum up, we have successfully synthesized different phases of high-entropy rare-earth zirconates, counterparts of starting ceria-zirconia compounds, using a modified sol-gel method. In order to obtain κ-Ce$_2$Zr$_2$O$_8$ and κ-(La$_{0.2}$Ce$_{0.2}$Pr$_{0.2}$Gd$_{0.2}$Y$_{0.2}$)$_2$Zr$_2$O$_{7+\delta}$ partially oxidized pyrochlore phase, high temperature reduction of starting solid solutions at 1500 °C, Ce$_{0.5}$Zr$_{0.5}$O$_2$ and La$_{0.1}$Ce$_{0.1}$Pr$_{0.1}$Gd$_{0.1}$Y$_{0.1}$Zr$_{0.5}$O$_2$, using hydrogen was needed. In this manner, pyrochlore phases, p-Ce$_2$Zr$_2$O$_7$ and p-(La$_{0.2}$Ce$_{0.2}$Pr$_{0.2}$Gd$_{0.2}$Y$_{0.2}$)$_2$Zr$_2$O$_7$, were formed, followed by mild re-oxidation of them at 600 °C. These six samples were structurally characterized using PXRD, Raman spectroscopy, SEM-EDS, and BET specific surface area. According to Rietveld refinement, all three samples that consist only of cerium atoms on the A site and zirconium atoms on the B site show a single-phase structure. In the case of high-entropy counterparts, the starting solid solution showed remarkable similarities with the starting solid solution Ce$_{0.5}$Zr$_{0.5}$O$_2$. When talking about the pyrochlore phase, it was concluded that it exhibits a pyrochlore-fluorite dual phase, and that there is 37.41 wt. % of pyrochlore and 62.59 wt. % of fluorite phase. Interestingly, Rietveld refinement after temperature-programmed desorption of carbon dioxide showed that p-LCPGY is no longer a dual-phase but a pure single pyrochlore phase. In the literature mentioned above, the main criteria that must be satisfied are radius ratio, oxidation states, and atomic size disorder. Herein, it is visible that using 5% CH$_4$/Ar helps obtain a single pyrochlore phase, which means that the reduction time of 10 h and temperature of 1500 °C might not be enough to synthesize a single-phase pyrochlore compound despite all of the criteria being met. When talking about the kappa phase, all of the rare-earth cations on the A site have to be oxidized to the +4 state, and the only cations that undergo such a reaction are Ce^{3+} and Pr^{3+}. We proposed two crystal structures of newly formed κ-(La$_{0.2}$Ce$_{0.2}$Pr$_{0.2}$Gd$_{0.2}$Y$_{0.2}$)$_2$Zr$_2$O$_{7+\delta}$ after re-oxidation, partially oxidized pyrochlore phase, and partially oxidized kappa phase. Considering this assumption, the Rietveld refinement was performed for both cases. Since only these two cations have the ability to change oxidation state to +4, we expect the 8b position to be only partially filled during re-oxidation of p-(La$_{0.2}$Ce$_{0.2}$Pr$_{0.2}$Gd$_{0.2}$Y$_{0.2}$)$_2$Zr$_2$O$_7$. According to the Rietveld refinement results, a better fit was obtained for the $Fd–3m$ space group and showed no peak splitting at higher 2θ angles, which is proof of obtaining single-phase partially oxidized pyrochlore (La$_{0.2}$Ce$_{0.2}$Pr$_{0.2}$Gd$_{0.2}$Y$_{0.2}$)$_2$Zr$_2$O$_{7+\delta}$. These results correspond to Raman spectroscopy data, which have shown similar scattering signals for both p-(La$_{0.2}$Ce$_{0.2}$Pr$_{0.2}$Gd$_{0.2}$Y$_{0.2}$)$_2$Zr$_2$O$_7$ and so-called κ-(La$_{0.2}$Ce$_{0.2}$Pr$_{0.2}$Gd$_{0.2}$Y$_{0.2}$)$_2$Zr$_2$O$_8$. The scattering signal at around 2150 cm^{-1} is characteristic only of the pyrochlore form, which is evidence that only pyrochlore-type compounds are Ce^{3+}-based. Another evidence is that from TGA, comparing p-CeZrO and p-LCPGY in an oxidative atmosphere, only p-CeZrO has an
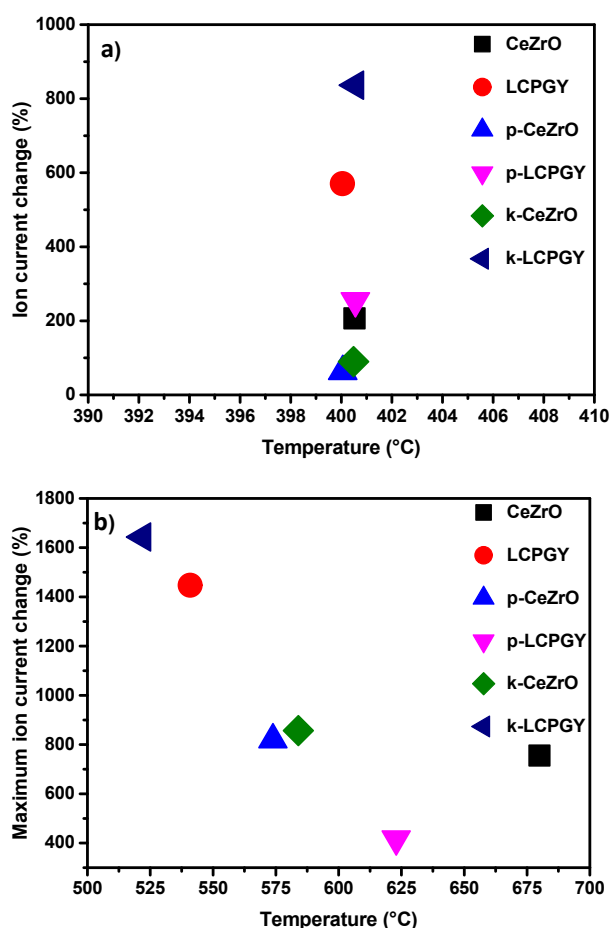
enormous mass change of 2.2% which can be the result of oxidation of Ce^{3+} to Ce^{4+}, i.e. kappa phase formation. Regarding methane oxidation, the greatest results showed high-entropy forms, solid solution LCPGY and κ-LCPGY (partially oxidized pyrochlore phase). This would mean that they produce larger amounts of carbon dioxide than other forms since structural analysis showed that they possess a larger amount of oxygen at the surface i.e. larger oxygen storage capacity (OSC). After the methane oxidation, κ-LCPGY (partially oxidized pyrochlore Fd–$3m$, kept the same amount of incorporated oxygen (68 %) at the 8b position, showing its reusability and productiveness in catalytic oxidation reactions. Another thing is that all other rare-earth elements can be successfully incorporated into the CeO_2-ZrO_2 system and thereby increase catalytic activity. Even though our conclusions form a solid framework, more in-depth research is needed to smoothly obtain a single-phase structure, maximize the efficiency of these catalysts, and diversify their applications.

Author contributions

S. Š. synthesis, conceptualization, original draft preparation; D. T. XRD measurements and formal analysis; T. S. SEM-EDS measurements and elemental mapping, TPD measurements and analysis; C. B. P. Raman spectroscopy measurements and analysis; I. S. EDS elemental quantification; M. F. XPS measurements; I. Dj. project management funding acquisition; Á. K., M. M., and I Dj. review & editing; J.K. conceptualization, formal analysis, review & editing.

Conflicts of interest

There are no conflicts to declare.

Data availability

The data supporting this article have been included as part of the Supplementary Information.

Funding

Acknowledgments

References

1   P. Li, X. Chen, Y. Li and J. W. Schwank, A review on oxygen storage capacity of CeO2-based materials: Influence factors, measurement techniques, and applications in reactions related to catalytic automotive emissions control, *Catal Today*, 2019, **327**, 90–115.

2   M. Mogensen, Physical, chemical and electrochemical properties of pure and doped ceria, *Solid State Ion*, 2000, **129**, 63–94.

3   J. Kašpar and P. Fornasiero, Nanostructured materials for advanced automotive de-pollution catalysts, *J Solid State Chem*, 2003, **171**, 19–29.

4   T. Montini, M. Melchionna, M. Monai and P. Fornasiero, Fundamentals and Catalytic Applications of CeO $_2$ -Based Materials, *Chem Rev*, 2016, **116**, 5987–6041.

5   S. Das, J. M. Dowding, K. E. Klump, J. F. McGinnis, W. Self and S. Seal, Cerium Oxide Nanoparticles: Applications and Prospects in Nanomedicine, *Nanomedicine*, 2013, **8**, 1483–1508.

6   P. Li, L. Fang, N. Hou, J. Li, X. Yao, T. Gan, L. Fan, Y. Zhao and Y. Li, Improved Performance of Ni-Mo Based Anode for Direct Methanol Solid Oxide Fuel Cells with the Addition of Rare Earth Oxides, *J Electrochem Soc*, 2017, **164**, F1142–F1148.

7   T. Montini, N. Hickey, P. Fornasiero, M. Graziani, M. A. Bañares, M. V. Martinez-Huerta, I. Alessandri and L. E. Depero, Variations in the Extent of Pyrochlore-Type Cation Ordering in Ce $_2$ Zr $_2$ O $_8$: A t'−κ Pathway to Low-Temperature Reduction, *Chemistry of Materials*, 2005, **17**, 1157–1166.

8   D. R. Sellick, A. Aranda, T. García, J. M. López, B. Solsona, A. M. Mastral, D. J. Morgan, A. F. Carley and S. H. Taylor, Influence of the preparation method on the activity of ceria zirconia mixed oxides for naphthalene total oxidation, *Appl Catal B*, 2013, **132–133**, 98–106.

9   G. Zhou, W.-T. Geng, W. Xiao, L. Sun, J. Wang and L. Wang, Thermal stability of zirconia-doped ceria surfaces: A first-principles molecular dynamics study, *Appl Surf Sci*, 2020, **507**, 144942.

10   C. Hori, Thermal stability of oxygen storage properties in a mixed CeO2-ZrO2 system, *Appl Catal B*, 1998, **16**, 105–117.

11   T. Sasaki, Y. Ukyo, K. Kuroda, S. Arai, S. Muto and H. Saka, Crystal Structure of Ce2Zr2O7 and .BETA.-Ce2Zr2O7.5, *Journal of the Ceramic Society of Japan*, 2004, **112**, 440–444.

12   S. Otsuka-Yao-Matsuo, T. Omata, N. Izu and H. Kishimoto, Oxygen Release Behavior of CeZrO4Powders and Appearance of New Compoundsκand t*, *J Solid State Chem*, 1998, **138**, 47–54.

13   A. Suda, Y. Ukyo, K. Yamamura, H. Sobukawa, T. Sasaki, Y. Nagai, T. Tanabe and M. Sugiura, Effect of Ordered Arrangement of Ce and Zr Ions on Oxygen Storage

Capacity of Ceria-Zirconia Solid Solution, *Journal of the Ceramic Society of Japan*, 2004, **112**, 586–589.

14   S. Urban, P. Dolcet, M. Möller, L. Chen, P. J. Klar, I. Djerdj, S. Gross, B. M. Smarsly and H. Over, Synthesis and full characterization of the phase-pure pyrochlore Ce2Zr2O7 and the κ-Ce2Zr2O8 phases, *Appl Catal B*, 2016, **197**, 23–34.

15   S. Urban, I. Djerdj, P. Dolcet, L. Chen, M. Möller, O. Khalid, H. Camuka, R. Ellinghaus, C. Li, S. Gross, P. J. Klar, Bernd Smarsly and H. Over, In Situ Study of the Oxygen-Induced Transformation of Pyrochlore Ce 2 Zr 2 O 7+ x to the κ-Ce 2 Zr 2 O 8 Phase, *Chemistry of Materials*, 2017, **29**, 9218–9226.

16   C. M. Rost, E. Sachet, T. Borman, A. Moballegh, E. C. Dickey, D. Hou, J. L. Jones, S. Curtarolo and J. P. Maria, Entropy-stabilized oxides, *Nat Commun*, DOI:10.1038/ncomms9485.

17   S. Šarić, J. Kojčinović, D. Tatar and I. Djerdj, Overview of Recent Advances in Rare-Earth High-Entropy Oxides as Multifunctional Materials for Next-Gen Technology Applications, *Molecules*, 2025, **30**, 1082.

18   P. R. Jothi, W. Liyanage, B. Jiang, S. Paladugu, D. Olds, D. A. Gilbert and K. Page, Persistent Structure and Frustrated Magnetism in High Entropy Rare-Earth Zirconates, *Small*, DOI:10.1002/smll.202101323.

19   H. Fu, Y. Jiang, M. Zhang, Z. Zhong, Z. Liang, S. Wang, Y. Du and C. Yan, High-entropy rare earth materials: synthesis, application and outlook, *Chem Soc Rev*, 2024, **53**, 2211–2247.

20   B. Matović, D. Zagorac, I. Cvijović-Alagić, J. Zagorac, S. Butulija, J. Erčić, O. Hanzel, R. Sedlák, M. Lisnichuk and P. Tatarko, Fabrication and characterization of high entropy pyrochlore ceramics, *Boletín de la Sociedad Española de Cerámica y Vidrio*, 2023, **62**, 66–76.

21   F. Li, L. Zhou, J.-X. Liu, Y. Liang and G.-J. Zhang, High-entropy pyrochlores with low thermal conductivity for thermal barrier coating materials, *Journal of Advanced Ceramics*, 2019, **8**, 576–582.

22   Y. Wang, Y. J. Jin, T. Wei, Z. G. Wang, G. Cao, Z. Y. Ding, Z. G. Liu, J. H. Ouyang, Y. J. Wang and Y. M. Wang, Size disorder: A descriptor for predicting the single- or dual-phase formation in multi-component rare earth zirconates, *J Alloys Compd*, DOI:10.1016/j.jallcom.2022.165636.

23   J. He, G. He, P. Wang, L. Xu, J. Liu and J. Tao, Pyrochlore–fluorite dual-phase high-entropy RE2(Ce0.2Zr0.2Hf0.2Sn0.2Ti0.2)2O7 (RE2HE2O7, RE = La, Nd, Sm, Eu, Gd, Dy) ceramics with glass-like thermal conductivity, *J Mater Sci*, DOI:10.1007/s10853-022-07734-3.

24   C. M. Rost, E. Sachet, T. Borman, A. Moballegh, E. C. Dickey, D. Hou, J. L. Jones, S. Curtarolo and J.-P. Maria, Entropy-stabilized oxides, *Nat Commun*, 2015, **6**, 8485.

25   A. Sarkar, Q. Wang, A. Schiele, M. R. Chellali, S. S. Bhattacharya, D. Wang, T. Brezesinski, H. Hahn, L. Velasco and B. Breitung, High-Entropy Oxides: Fundamental Aspects and Electrochemical Properties, *Advanced Materials*, 2019, **31**, 1806236.

26   F. X. Zhang, M. Lang and R. C. Ewing, Atomic disorder in Gd2Zr2O7 pyrochlore, *Appl Phys Lett*, DOI:10.1063/1.4921268.

27   Y. Wang, Y.-J. Jin, T. Wei, Z.-G. Wang, G. Cao, Z.-Y. Ding, Z.-G. Liu, J. Ouyang, Y.-J. Wang and Y. Wang, Size Disorder: A Descriptor for Predicting the Single- or Dual-Phase Formation in Multi-Component Rare Earth Zirconates, *SSRN Electronic Journal*, DOI:10.2139/ssrn.4084603.

28   G. N. Kotsonis, S. S. I. Almishal, L. Miao, M. K. Caucci, G. R. Bejger, S. V. G. Ayyagari, T. W. Valentine, B. E. Yang, S. B. Sinnott, C. M. Rost, N. Alem and J.-P. Maria, Fluorite-structured high-entropy oxide sputtered thin films from bixbyite target, *Appl Phys Lett*, DOI:10.1063/5.0201419.

29   G. R. Bejger, M. K. Caucci, S. S. I. Almishal, B. Yang, J.-P. Maria, S. B. Sinnott and C. M. Rost, Lanthanide L-edge spectroscopy of high-entropy oxides: insights into valence and phase stability, *J Mater Chem A Mater*, DOI:10.1039/D5TA03815D.

30   A. Sarkar, C. Loho, L. Velasco, T. Thomas, S. S. Bhattacharya, H. Hahn and R. Djenadic, Multicomponent equiatomic rare earth oxides with a narrow band gap and associated praseodymium multivalency, *Dalton Transactions*, 2017, **46**, 12167–12176.

31   L. Spiridigliozzi, V. Monfreda, A. Marocco and G. Dell'Agli, On the effect of kinetics on the formation of fluorite/bixbyite-structured Entropy-Stabilized Oxides, *Ceram Int*, 2025, **51**, 30684–30692.

32   A. Bergerud, S. M. Selbach and D. J. Milliron, Oxygen Incorporation and Release in Metastable Bixbyite V 2 O 3 Nanocrystals, *ACS Nano*, 2016, **10**, 6147–6155.

33   A. Sarkar, B. Eggert, L. Velasco, X. Mu, J. Lill, K. Ollefs, S. S. Bhattacharya, H. Wende, R. Kruk, R. A. Brand and H. Hahn, Role of intermediate 4 *f* states in tuning the band structure of high entropy oxides, *APL Mater*, DOI:10.1063/5.0007944.

34   J. Chen, B. D. Carlson, T. J. Toops, Z. Li, M. J. Lance, S. G. Karakalos, J. Choi and E. A. Kyriakidou, Methane Combustion Over Ni/Ce _x Zr _1–x O _2 Catalysts: Impact of Ceria/Zirconia Ratio, *ChemCatChem*, 2020, **12**, 5558–5568.

35   E. Smal, Y. Bespalko, M. Arapova, V. Fedorova, K. Valeev, N. Eremeev, E. Sadovskaya, T. Krieger, T. Glazneva, V. Sadykov and M. Simonov, Carbon Formation during Methane Dry Reforming over Ni-Containing Ceria-Zirconia Catalysts, *Nanomaterials*, 2022, **12**, 3676.

36   M. Gil-Calvo, C. Jiménez-González, B. de Rivas, J. I. Gutiérrez-Ortiz and R. López-Fonseca, Novel Nickel Aluminate-Derived Catalysts Supported on Ceria and Ceria–Zirconia for Partial Oxidation of Methane, *Ind Eng Chem Res*, 2017, **56**, 6186–6197.

37   Y. Lyu, J. N. Jocz, R. Xu, O. C. Williams and C. Sievers, Selective Oxidation of Methane to Methanol over Ceria-Zirconia Supported Mono and Bimetallic Transition Metal Oxide Catalysts, *ChemCatChem*, 2021, **13**, 2832–2842.

38   M. Arapova, E. Smal, Y. Bespalko, K. Valeev, V. Fedorova, A. Hassan, O. Bulavchenko, V. Sadykov and M. Simonov, Methane Dry Reforming Catalysts Based on Pr-Doped Ceria–Zirconia Synthesized in Supercritical Propanol, *Energies (Basel)*, 2023, **16**, 4729.

39   Y. Liu, S. Cen, C. Bu, D. Liu and G. Piao, Redox kinetics of ceria–zirconia (Ce _1–x Zr _x O _2–δ) for thermochemical partial oxidation of methane and H 2 O/CO 2 splitting at moderate temperature, *Sustain Energy Fuels*, 2024, **8**, 942–956.

40   R. Nedyalkova, D. Niznansky and A.-C. Roger, Iron–ceria–zirconia fluorite catalysts for methane selective oxidation to formaldehyde, *Catal Commun*, 2009, **10**, 1875–1880.

41   A. S. Larimi and S. M. Alavi, Ceria-Zirconia supported Ni catalysts for partial oxidation of methane to synthesis gas, *Fuel*, 2012, **102**, 366–371.

42   J. Bijelić, D. Tatar, M. Sahu, Z. Jagličić and I. Djerdj, Size reduction-induced properties modifications of antiferromagnetic dielectric nanocrystalline Ba2NiMO6 (M = W, Te) double perovskites, *Oxford Open Materials Science*, 2020, **1**, 1–9.

43 M. Sahu, S. Hajra, J. Bijelic, D. Oh, I. Djerdj and H. J. Kim, Triple perovskite-based triboelectric nanogenerator: a facile method of energy harvesting and self-powered information generator, *Mater Today Energy*, 2021, **20**, 100639.

44 J. Bijelić, A. Stanković, B. Matasović, B. Marković, M. Bijelić, Ž. Skoko, J. Popović, G. Štefanić, Z. Jagličić, S. Zellmer, T. Preller, G. Garnweitner, T. Đorđević, P. Cop, B. Smarsly and I. Djerdj, Structural characterization and magnetic property determination of nanocrystalline Ba $_3$ Fe $_2$ WO $_9$ and Sr $_3$ Fe $_2$ WO $_9$ perovskites prepared by a modified aqueous sol–gel route, *CrystEngComm*, 2019, **21**, 218–227.

45 J. Bijelić, D. Tatar, S. Hajra, M. Sahu, S. J. Kim, Z. Jagličić and I. Djerdj, Nanocrystalline Antiferromagnetic High-κ Dielectric Sr2NiMO6 (M = Te, W) with Double Perovskite Structure Type, *Molecules*, 2020, **25**, 3996.

46 J. Bijelić, A. Stanković, M. Medvidović-Kosanović, B. Marković, P. Cop, Y. Sun, S. Hajra, M. Sahu, J. Vukmirović, D. Marković, Á. Kukovecz, Z. Jagličić, B. M. Smarsly and I. Djerdj, Rational Sol–Gel-Based Synthesis Design and Magnetic, Dielectric, and Optical Properties Study of Nanocrystalline Sr $_3$ Co $_2$ WO $_9$ Triple Perovskite, *The Journal of Physical Chemistry C*, 2020, **124**, 12794–12807.

47 D. Tatar, J. Kojčinović, B. Marković, A. Széchenyi, A. Miletić, S. B. Nagy, S. Ziegenheim, I. Szenti, A. Sapi, Á. Kukovecz, K. Dinjar, Y. Tang, D. Stenzel, G. Varga and I. Djerdj, Sol-Gel Synthesis of Ceria-Zirconia-Based High-Entropy Oxides as High-Promotion Catalysts for the Synthesis of 1,2-Diketones from Aldehyde, *Molecules*, 2021, **26**, 6115.

48 D. Tatar, H. Ullah, M. Yadav, J. Kojčinović, S. Šarić, I. Szenti, T. Skalar, M. Finšgar, M. Tian, Á. Kukovecz, Z. Kónya, A. Sápi and I. Djerdj, High-Entropy Oxides: A New Frontier in Photocatalytic CO $_2$ Hydrogenation, *ACS Appl Mater Interfaces*, 2024, **16**, 29946–29962.

49 J. Rodriguez-Carvajal, FULLPROF: A Program for Rietveld Refinement and Pattern Matching Analysis, *Abstracts of the Satellite Meeting on Powder Diffraction of the XV Congress of the IUCr*, 1990, 127.

50 K. Momma and F. Izumi, VESTA : a three-dimensional visualization system for electronic and structural analysis, *J Appl Crystallogr*, 2008, **41**, 653–658.

51 Database of Ionic Radii, http://abulafia.mt.ic.ac.uk/shannon/ptable.php.

52 M. Glerup, O. F. Nielsen and F. W. Poulsen, The Structural Transformation from the Pyrochlore Structure, A2B2O7, to the Fluorite Structure, AO2, Studied by Raman Spectroscopy and Defect Chemistry Modeling, *J Solid State Chem*, 2001, **160**, 25–32.

53 T. Taniguchi, T. Watanebe, S. Ichinohe, M. Yoshimura, K. Katsumata, K. Okada and N. Matsushita, Nanoscale heterogeneities in CeO2–ZrO2 nanocrystals highlighted by UV-resonant Raman spectroscopy, *Nanoscale*, 2010, **2**, 1426.

54 E. Kroumova, M. I. Aroyo, J. M. Perez-Mato, A. Kirov, C. Capillas, S. Ivantchev and H. Wondratschek, Bilbao Crystallographic Server : Useful Databases and Tools for Phase-Transition Studies, *Phase Transitions*, 2003, **76**, 155–170.

55 P. Cop, R. Maile, Y. Sun, O. Khalid, I. Djerdj, P. Esch, S. Heiles, H. Over and B. M. Smarsly, Impact of Aliovalent/Isovalent Ions (Gd, Zr, Pr, and Tb) on the Catalytic Stability of Mesoporous Ceria in the HCl Oxidation Reaction, *ACS Appl Nano Mater*, 2020, **3**, 7406–7419.

56 X. Luo, L. Luo, X. Zhao, H. Cai, S. Duan, C. Xu, S. Huang, H. Jin and S. Hou, Single-phase rare-earth high-entropy zirconates with superior thermal and mechanical properties, *J Eur Ceram Soc*, 2022, **42**, 2391–2399.

57 J. R. McBride, K. C. Hass, B. D. Poindexter and W. H. Weber, Raman and x-ray studies of Ce1– *x* RE *x* O2– *y* , where RE=La, Pr, Nd, Eu, Gd, and Tb, *J Appl Phys*, 1994, **76**, 2435–2441.

58 V. M. Orera, R. I. Merino and F. Peña, Ce3+↔Ce4+ conversion in ceria-doped zirconia single crystals induced by oxido-reduction treatments, *Solid State Ion*, 1994, **72**, 224–231.

59 V. M. Orera, R. I. Merino and F. Peña, Ce3+↔Ce4+ conversion in ceria-doped zirconia single crystals induced by oxido-reduction treatments, *Solid State Ion*, 1994, **72**, 224–231.

60 D. Avisar and T. Livneh, The Raman-scattering of A-type Ce2O3, *Vib Spectrosc*, 2016, **86**, 14–16.

61 T. Otake, Ce3+ concentration in ZrO2–CeO2–Y2O3 system studied by electronic Raman scattering, *Solid State Ion*, 2000, **135**, 663–667.

62 E. Sartoretti, C. Novara, F. Giorgis, M. Piumetti, S. Bensaid, N. Russo and D. Fino, In situ Raman analyses of the soot oxidation reaction over nanostructured ceria-based catalysts, *Sci Rep*, 2019, **9**, 3875.

63 M. Smith, L. Scudiero, J. Espinal, J.-S. McEwen and M. Garcia-Perez, Improving the deconvolution and interpretation of XPS spectra from chars by ab initio calculations, *Carbon N Y*, 2016, **110**, 155–171.

64 X. Garcia, L. Soler, N. J. Divins, X. Vendrell, I. Serrano, I. Lucentini, J. Prat, E. Solano, M. Tallarida, C. Escudero and J. Llorca, Ceria-Based Catalysts Studied by Near Ambient Pressure X-ray Photoelectron Spectroscopy: A Review, *Catalysts*, 2020, **10**, 286.

65 L. H. Grey, H.-Y. Nie and M. C. Biesinger, Defining the nature of adventitious carbon and improving its merit as a charge correction reference for XPS, *Appl Surf Sci*, 2024, **653**, 159319.

66 Y. Uwamino, T. Ishizuka and H. Yamatera, X-ray photoelectron spectroscopy of rare-earth compounds, *J Electron Spectros Relat Phenomena*, 1984, **34**, 67–78.

67 S. R. Sanivarapu, J. B. Lawrence and G. Sreedhar, Role of Surface Oxygen Vacancies and Lanthanide Contraction Phenomenon of Ln(OH) $_3$ (Ln = La, Pr, and Nd) in Sulfide-Mediated Photoelectrochemical Water Splitting, *ACS Omega*, 2018, **3**, 6267–6278.

68 J. P. H. Li, X. Zhou, Y. Pang, L. Zhu, E. I. Vovk, L. Cong, A. P. van Bavel, S. Li and Y. Yang, Understanding of binding energy calibration in XPS of lanthanum oxide by *in situ* treatment, *Physical Chemistry Chemical Physics*, 2019, **21**, 22351–22358.

69 T. Gougousi, D. Niu, R. W. Ashcraft and G. N. Parsons, Carbonate formation during post-deposition ambient exposure of high-k dielectrics, *Appl Phys Lett*, 2003, **83**, 3543–3545.

70 M. Shaw, D. Samanta, S. Bera, M. K. Mahto, M. A. Salam Shaik, S. Konar, I. Mondal, D. Dhara and A. Pathak, Role of Surface Oxygen Vacancies and Oxygen Species on CuO Nanostructured Surfaces in Model Catalytic Oxidation and Reductions: Insight into the Structure–Activity Relationship Toward the Performance, *Inorg Chem*, 2022, **61**, 14568–14581.

71 J. Landoulsi, M. J. Genet, S. Fleith, Y. Touré, I. Liascukiene, C. Méthivier and P. G. Rouxhet, Organic adlayer on inorganic materials: XPS analysis selectivity to cope with adventitious contamination, *Appl Surf Sci*, 2016, **383**, 71–83.

72 J. Kojčinović, D. Tatar, S. Šarić, C. Bartus Pravda, A. Mavrič, I. Arčon, Z. Jagličić, M. Mellin, M. Einert, A. Altomare, R. Caliandro, Á. Kukovecz, J. P. Hofmann and I.

CrystEngComm Accepted Manuscript

Djerdj, Resolving a structural issue in cerium-nickel-based oxide: a single compound or a two-phase system?, *Dalton Transactions*, 2024, **53**, 2082–2097.

73 D. R. Mullins, The surface chemistry of cerium oxide, *Surf Sci Rep*, 2015, **70**, 42–85.

74 M. Romeo, K. Bak, J. El Fallah, F. Le Normand and L. Hilaire, XPS Study of the reduction of cerium dioxide, *Surface and Interface Analysis*, 1993, **20**, 508–512.

75 M. Grünbacher, L. Schlicker, M. F. Bekheet, A. Gurlo, B. Klötzer and S. Penner, H_2 reduction of Gd- and Sm-doped ceria compared to pure CeO_2 at high temperatures: effect on structure, oxygen nonstoichiometry, hydrogen solubility and hydroxyl chemistry, *Physical Chemistry Chemical Physics*, 2018, **20**, 22099–22113.

76 H. Borchert, Y. V. Frolova, V. V. Kaichev, I. P. Prosvirin, G. M. Alikina, A. I. Lukashevich, V. I. Zaikovskii, E. M. Moroz, S. N. Trukhan, V. P. Ivanov, E. A. Paukshtis, V. I. Bukhtiyarov and V. A. Sadykov, Electronic and Chemical Properties of Nanostructured Cerium Dioxide Doped with Praseodymium, *J Phys Chem B*, 2005, **109**, 5728–5738.

77 M. Yu. Sinev, G. W. Graham, L. P. Haack and M. Shelef, Kinetic and structural studies of oxygen availability of the mixed oxides $Pr_{1-x}M_xO_y$ (M = Ce, Zr), *J Mater Res*, 1996, **11**, 1960–1971.

78 R. Rajakumaran, R. Sukanya, S. M. Chen, R. Karthik, C. B. Breslin and P. M. Shafi, Synthesis and Characterization of Pyrochlore-Type Praseodymium Stannate Nanoparticles: An Effective Electrocatalyst for Detection of Nitrofurazone Drug in Biological Samples, *Inorg Chem*, 2021, **60**, 2464–2476.

79 J. Zhang, L. Shi, R. Tong and L. Yang, Highly Active Pyrochlore-Type Praseodymium Ruthenate Electrocatalyst for Efficient Acid–Water Oxidation, *ACS Appl Mater Interfaces*, DOI:10.1021/acsami.3c08908.

80 A. Yamuna, P. Sundaresan, S.-M. Chen and W.-L. Shih, Ultrasound assisted synthesis of praseodymium tungstate nanoparticles for the electrochemical detection of cardioselective β-blocker drug, *Microchemical Journal*, 2020, **159**, 105420.

81 M. A. Gondal, T. A. Fasasi, U. Baig and A. Mekki, Effects of Oxidizing Media on the Composition, Morphology and Optical Properties of Colloidal Zirconium Oxide Nanoparticles Synthesized via Pulsed Laser Ablation in Liquid Technique, *J Nanosci Nanotechnol*, 2018, **18**, 4030–4039.

82 S. R. Teeparthi, E. W. Awin and R. Kumar, Dominating role of crystal structure over defect chemistry in black and white zirconia on visible light photocatalytic activity, *Sci Rep*, 2018, **8**, 5541.

83 J. Zhu, Y. Zhu, W. Shen, Y. Wang, J. Han, G. Tian, P. Lei and B. Dai, Growth and characterization of yttrium oxide films by reactive magnetron sputtering, *Thin Solid Films*, 2011, **519**, 4894–4898.

84 M. Liu, W. Liu, X. Liu, Y. Ouyang, H. Hou, M. Lei and Z. Wei, Yttrium oxide as a Q-switcher for the near-infrared erbium-doped fiber laser, *Nanophotonics*, 2020, **9**, 2887–2894.

85 D. F. Mullica, C. K. C. Lok, H. O. Perkins and V. Young, X-ray photoelectron final-state screening in La(OH)$_3$: A multiplet structural analysis, *Phys Rev B*, 1985, **31**, 4039–4042.

86 F. de Groot, Multiplet effects in X-ray spectroscopy, *Coord Chem Rev*, 2005, **249**, 31–63.

87 D. Jana, S. Maikap, A. Prakash, Y.-Y. Chen, H.-C. Chiu and J.-R. Yang, Enhanced resistive switching phenomena using low-positive-voltage format and self-compliance IrO$_x$/GdO$_x$/W cross-point memories, *Nanoscale Res Lett*, 2014, **9**, 12.

88 G. Vijayaprasath, I. Habibulla, V. Dharuman, S. Balasubramanian and R. Ganesan, Fabrication of Gd_2O_3 Nanosheet-Modified Glassy Carbon Electrode for Nonenzymatic Highly Selective Electrochemical Detection of Vitamin B2, *ACS Omega*, 2020, **5**, 17892–17899.

89 T. ul Haq, S. A. Mansour, A. Munir and Y. Haik, Gold-Supported Gadolinium Doped CoB Amorphous Sheet: A New Benchmark Electrocatalyst for Water Oxidation with High Turnover Frequency, *Adv Funct Mater*, DOI:10.1002/adfm.201910309.

90 S. A. Hassanzadeh-Tabrizi, Precise calculation of crystallite size of nanomaterials: A review, *J Alloys Compd*, 2023, **968**, 171914.

91 A. J. Ruys, in *Silicon Carbide Ceramics*, Elsevier, 2023, pp. 349–394.

92 P. T. M. Nguyen, D. D. Do and D. Nicholson, On The Cavitation and Pore Blocking in Cylindrical Pores with Simple Connectivity, *J Phys Chem B*, 2011, **115**, 12160–12172.

93 M. Thommes and K. A. Cychosz, Physical adsorption characterization of nanoporous materials: progress and challenges, *Adsorption*, 2014, **20**, 233–250.

94 K. A. Cychosz, R. Guillet-Nicolas, J. García-Martínez and M. Thommes, Recent advances in the textural characterization of hierarchically structured nanoporous materials, *Chem Soc Rev*, 2017, **46**, 389–414.

95 N. Nhiem Dao and M. Dai Luu, Synthesis and investigations on CO catalytic oxidation activity of nanostructured $Ce_{0.5}Zr_{0.5}O_2$ prepared by combustion method using polyvinyl alcohol, *Advances in Natural Sciences: Nanoscience and Nanotechnology*, 2012, **3**, 015014.

96 A. Hadi, M. Nazri Abu Shah, K. N. Ismail and R. Ismail, Novel synthesis of high surface area nano-$CeZrO_2$: transformation of the microstructure and textural properties as the effect of calcination, *Advances in Natural Sciences: Nanoscience and Nanotechnology*, 2018, **9**, 045015.

97 E. P. Barrett, L. G. Joyner and P. P. Halenda, The Determination of Pore Volume and Area Distributions in Porous Substances. I. Computations from Nitrogen Isotherms, *J Am Chem Soc*, 1951, **73**, 373–380.

98 S. Storck, H. Bretinger and W. F. Maier, Characterization of micro- and mesoporous solids by physisorption methods and pore-size analysis, *Appl Catal A Gen*, 1998, **174**, 137–146.

99 A. E. Baranchikov, O. S. Polezhaeva, V. K. Ivanov and Y. D. Tretyakov, Lattice expansion and oxygen non-stoichiometry of nanocrystalline ceria, *CrystEngComm*, 2010, **12**, 3531.

100 X. Liu, H. Yang, L. Han, W. Liu, C. Zhang, X. Zhang, S. Wang and Y. Yang, Mesoporous-shelled CeO2 hollow nanospheres synthesized by a one-pot hydrothermal route and their catalytic performance, *CrystEngComm*, 2013, **15**, 7769.

101 C. Doornkamp and V. Ponec, The universal character of the Mars and Van Krevelen mechanism, *J Mol Catal A Chem*, 2000, **162**, 19–32.

102 D. Jiang, K. Khivantsev and Y. Wang, Low-Temperature Methane Oxidation for Efficient Emission Control in Natural Gas Vehicles: Pd and Beyond, *ACS Catal*, 2020, **10**, 14304–14314.

103 J. Kim, M. S. Abbott, D. B. Go and J. C. Hicks, Enhancing C–H Bond Activation of Methane via Temperature-

CrystEngComm Accepted Manuscript

Controlled, Catalyst–Plasma Interactions, *ACS Energy Lett*, 2016, **1**, 94–99.

104 Z. Cheng, D. S. Baser, S. G. Nadgouda, L. Qin, J. A. Fan and L.-S. Fan, C$_2$ Selectivity Enhancement in Chemical Looping Oxidative Coupling of Methane over a Mg–Mn Composite Oxygen Carrier by Li-Doping-Induced Oxygen Vacancies, *ACS Energy Lett*, 2018, **3**, 1730–1736.

105 P. Barboun, P. Mehta, F. A. Herrera, D. B. Go, W. F. Schneider and J. C. Hicks, Distinguishing Plasma Contributions to Catalyst Performance in Plasma-Assisted Ammonia Synthesis, *ACS Sustain Chem Eng*, 2019, **7**, 8621–8630.

106 P. Mehta, P. Barboun, D. B. Go, J. C. Hicks and W. F. Schneider, Catalysis Enabled by Plasma Activation of Strong Chemical Bonds: A Review, *ACS Energy Lett*, 2019, **4**, 1115–1133.

107 A. Hussain, Y. Zheng, Q. Wang and Y. Cui, Synthesis of high-entropy oxides derived from metal–organic frameworks and their catalytic performance for total toluene oxidation, *New Journal of Chemistry*, 2024, **48**, 17237–17245.

108 W. Zhang, T. Qi, W. Zhang, J. Yan, Z. Li, S. Kang, S. Ren, Z. Lei, Z. Wang and H. Shui, Enhancing the activity and sulfur tolerance of LaMnO3-based perovskite catalysts for VOCs total oxidation by tuning configurational entropy, *Sep Purif Technol*, 2025, **372**, 133433.

109 W. Zhang, W. Zhang, J. Yan, Z. Li, S. Kang, S. Ren, Z. Lei, Z. Wang and H. Shui, High-entropy CeZrCoMnNi oxide catalysts with defect-engineered synergy: Simultaneous boosting of activity, stability, and poisoning resistance for propane combustion, *J Environ Chem Eng*, 2025, **13**, 118450.

110 S. Nundy, D. Tatar, J. Kojčinović, H. Ullah, A. Ghosh, T. K. Mallick, R. Meinusch, B. M. Smarsly, A. A. Tahir and I. Djerdj, Bandgap Engineering in Novel Fluorite-Type Rare Earth High-Entropy Oxides (RE-HEOs) with Computational and Experimental Validation for Photocatalytic Water Splitting Applications, *Adv Sustain Syst*, 2022, **6**, 2200067.

111 T. X. Nguyen, Y. Liao, C. Lin, Y. Su and J. Ting, Advanced High Entropy Perovskite Oxide Electrocatalyst for Oxygen Evolution Reaction, *Adv Funct Mater*, DOI:10.1002/adfm.202101632.

112 T. Wang, H. Chen, Z. Yang, J. Liang and S. Dai, High-Entropy Perovskite Fluorides: A New Platform for Oxygen Evolution Catalysis, *J Am Chem Soc*, 2020, **142**, 4550–4554.

113 D. Stenzel, B. Zhou, C. Okafor, M. V. Kante, L. Lin, G. Melinte, T. Bergfeldt, M. Botros, H. Hahn, B. Breitung and S. Schweidler, High-entropy spinel-structure oxides as oxygen evolution reaction electrocatalyst, *Front Energy Res*, DOI:10.3389/fenrg.2022.942314.

114 F. Liu, M. Yu, X. Chen, J. Li, H. Liu and F. Cheng, Defective high-entropy rocksalt oxide with enhanced metal–oxygen covalency for electrocatalytic oxygen evolution, *Chinese Journal of Catalysis*, 2022, **43**, 122–129.

115 K. Iwase and I. Honma, High-Entropy Spinel Oxide Nanoparticles Synthesized via Supercritical Hydrothermal Processing as Oxygen Evolution Electrocatalysts, *ACS Appl Energy Mater*, 2022, **5**, 9292–9296.

116 Y. Zhang, W. Dai, P. Zhang, T. Lu and Y. Pan, In-situ electrochemical tuning of (CoNiMnZnFe)3O3.2 high-entropy oxide for efficient oxygen evolution reactions, *J Alloys Compd*, 2021, **868**, 159064.

117 K.-H. Kim and Y.-H. Choi, Effect of constituent cations on the electrocatalytic oxygen evolution reaction in high-entropy oxide (Mg0.2Fe0.2Co0.2Ni0.2Cu0.2)O, *Journal of Electroanalytical Chemistry*, 2022, **922**, 116737.

118 X. Ji, F. Yang, Y. Du, J. Li, J. Li and Q. Hu, Highly active and durable La0.6Ca0.4(CrMnFeCo2Ni)O3 high entropy perovskite oxide as electrocatalyst for oxygen evolution reaction in alkaline media, *J Mater Sci Technol*, 2024, **168**, 71–78.

119 S. H. Albedwawi, A. AlJaberi, G. N. Haidemenopoulos and K. Polychronopoulou, High entropy oxides-exploring a paradigm of promising catalysts: A review, *Mater Des*, 2021, **202**, 109534.

120 D. Tatar, H. Ullah, M. Yadav, J. Kojčinović, S. Šarić, I. Szenti, T. Skalar, M. Finšgar, M. Tian, Á. Kukovecz, Z. Kónya, A. Sápi and I. Djerdj, High-Entropy Oxides: A New Frontier in Photocatalytic CO$_2$ Hydrogenation, *ACS Appl Mater Interfaces*, 2024, **16**, 29946–29962.

121 M. H. Khedr, K. S. A. Halim, M. I. Nasr and A. M. El-Mansy, Effect of temperature on the catalytic oxidation of CO over nano-sized iron oxide, *Materials Science and Engineering: A*, 2006, **430**, 40–45.

View Article Online
DOI: 10.1039/D5CE00736D

Data availability statement (DAS)

for

From solid solution towards pyrochlore and kappa phases: introducing configurational entropy in ordered ceria-zirconia systems

Stjepan Šarić[a], Dalibor Tatar[a], Tina Skalar[b], Marjan Marinšek[b], Cora Bartus Pravda[c], Ákos Kukovecz[c], Imre Szenti[c], Matjaž Finšgar[d], Igor Djerdj[a] and Jelena Kojčinović[a,*]

[a] *Department of Chemistry, Josip Juraj Strossmayer University of Osijek, Cara Hadrijana 8/A, 31000 Osijek, Croatia*

[b] *Faculty of Chemistry and Chemical Technology, Večna pot 113, 1000 Ljubljana, Slovenia*

[c] *Department of Applied and Environmental Chemistry, University of Szeged, 6720 Szeged, Hungary*

[d] *Faculty of Chemistry and Chemical Engineering, University of Maribor, Maribor Smetanova 17, 2000, Slovenia*

*jbijelic@kemija.unios.hr

The data supporting this article have been included as part of the Supplementary Information file. This statement has been included at the end of the main article.

Sincerely,

The Authors